General Disclaimer

One or more of the Following Statements may affect this Document

- This document has been reproduced from the best copy furnished by the organizational source. It is being released in the interest of making available as much information as possible.

- This document may contain data, which exceeds the sheet parameters. It was furnished in this condition by the organizational source and is the best copy available.

- This document may contain tone-on-tone or color graphs, charts and/or pictures, which have been reproduced in black and white.

- This document is paginated as submitted by the original source.

- Portions of this document are not fully legible due to the historical nature of some of the material. However, it is the best reproduction available from the original submission.

Studies of Oceanic Tectonics Based on GEOS-3 Satellite Altimetry

K.A. Foehls, W.M. Kaula, G. Schubert, and D. Sandwell

April 1979

NASA

National Aeronautics and
Space Administration

Wallops Flight Center
Wallops Island, Virginia 23337
AC 804 824-3411

Studies of Oceanic Tectonics Based on GEOS-3 Satellite Altimetry

K.A. Poehls, W.M. Kaula, G. Schubert, and D. Sandwell
Department of Earth and Space Sciences
University of California
Los Angeles, California 90024

CONTENTS

1. INTRODUCTION

The GEOS-3 investigations at UCLA originally proposed a mixture of geoid determination and geophysical analysis and interpretation. While efforts in all these directions were undertaken, it has become apparent that, taking into account work elsewhere, the area in which we could most significantly contribute is the analysis and interpretation, which is therefore emphasized in this report.

Variations in the external gravity field--expressed either as geoid undulations or gravity anomalies--indicate, of course, lateral variations in density within the solid earth. In any laterally coherent material, such density variations must entail shear stresses. The finite strength of rocks limits these stresses; there will always be fracture and flow until the density variations are removed or compensated in some way. Because (1) this flow has a rate highly non-linear in stress; (2) the rheological properties of rocks are strongly temperature dependent; and (3) the stress for a given amplitude of density irregularity is proportionate to the wavelength, we should expect even the relatively plastic oceanic lithosphere and upper mantle to show a gravity signal whose broad wavelengths correspond to isostatic compensation of the rise to basin topographic drop around asthenospheric depth, but whose local variations indicate departures from this overall "$t^{\frac{1}{2}}$" sweep. This oceanic isostasy differs from the more familiar continental variety in that it is mainly thermal, rather than compositional, in origin: in general, there is a positive correlation of temperature with topography, hence a negative correlation of density with topography, such that the total mass of a column of matter down to somewhere around the asthenosphere is about the same everywhere. Models of thermal convection define the distribution of this isostatic compensation. Since, in principle, pressure effects can result in differences from this equal loading, perhaps the term 'isodynamics' should be used rather than 'isostasy'. But these differences are small in models developed so far.

Given the foregoing considerations, together with the likelihood that features deeper in the mantle not connected in an obvious way to plate tectonics are contributing to the gravity signal, any rational procedure of analyzing or interpreting the ocean geoid and topography will take into account their spectra. Procedures which have been applied can be classified are varying mixtures of four archetypes: (1) statistical analyses, in which auto- and cross-covariances and their spectral transforms, or admittances, are determined from gravimetry and bathymetry (e.g., McKenzie & Bowin, 1976; Kaula, 1977); (2) removal of empirically determined mean trends and mapping of residuals (e.g., Sclater et al., 1975; Cochran & Talwani, 1977); (3) direct modelling in which the effects of

a specified thermal and mechanical model on observables are calculated (e.g., McKenzie et al., 1974; Schubert et al., 1976); and (4) inverse modelling, in which the best values for the parameters of a specified model are inferred from data (e.g., Burkhard & Jackson, 1977). At present levels of data coverage, technique, and insight, any particular study is a trade-off between the different aspects: elaborate statistical analyses assume rather simple interior models, while complex physical models account for only certain features of the data. We discuss here efforts in categories (1) and (3) in turn: statistical analyses and lithospheric-asthenospheric modelling. As will be seen, the necessity of removing effects of orbital errors from altimetry make statistical analyses willy-nilly incorporate (2), removal of empirically determined trends.

2. STATISTICAL ANALYSES

2.1 Admittance Analysis Fundamentals

McKenzie (1967) suggested that the relationship between gravity (or geoid) anomalies and topography should be analyzed in terms of the admittance. If the gravity anomalies Δg and ocean depths b along a track are expressed in terms of complex Fourier series,

$$\left. \begin{aligned} \Delta g &= \sum_k g(k) e^{ikx} \\ b &= \sum_k b(k) e^{ikx} \end{aligned} \right\} , \tag{2.1}$$

where x is along-track location and k is the wave number, then, if there are no other density irregularities than the topography, the complex admittance $Z(k)$ is defined by (McKenzie & Bowin, 1976):

$$g(k) = Z(k) b(k) \tag{2.2}$$

The first task is to estimate the admittance from the gravity and bathymetry over specific tracks, and the second to investigate what models produce admittances most closely approximating the observed admittance.

To estimate the admittance from N equal blocks of data, the mean and trend from each block r are removed by least squares, the Fourier transforms $g_r(k)$, $b_r(k)$ obtained, and the auto- and cross-power spectra determined from

$$\left. \begin{aligned} S_k(gg) \\ S_k(bb) \\ S_k(gb) \end{aligned} \right\} = \frac{1}{2N} \sum_{r=1}^{N} \left\{ \begin{aligned} g_r(k) g_r^*(k) \\ b_r(k) b_r^*(k) \\ g_r(k) b_r^*(k) \end{aligned} \right\} \tag{2.3}$$

where the asterik denotes the complex conjugate. The admittance is then obtained from

$$Z(k) = S_k(gb)/S_k(bb) \qquad (2.4)$$

The coherence $\gamma^2(k)$ is defined by

$$\gamma^2(k) = S_k(gb)S_k^*(gb)/S_k(gg)S_k(bb) \qquad (2.5)$$

All these functions can equally well be determined for geoid heights N as for gravity anomalies Δg, of course.

2.2 Geoid and Seafloor Bathymetry

We utilized the sea surface heights above the ellipsoid, corrected for tidal variations, produced by NASA Wallops Flight Center. A standard deviation of 0.1-0.3 m was commonly found for individual altitude measurements, although values of over 1 m may be found on bad passes. Measurements tended to be poorer over very calm seas or upon approaching land. This standard deviation of 0.1-0.3 m is probably representative of the relative accuracy of the measurements along an individual satellite pass. Orbit errors were indicated by large residuals at track crossings. From our work, the orbital errors appeared to have wavelengths of 10,000 km or more. The estimated relative standard deviations of 0.1-0.3 m is certainly small enough to resolve 3-6 m perturbations in the geoid along long tracks. Some problems may be experienced in determining areal geoids involving numerous tracks, however, if these long wavelength orbit analysis errors are not reduced.

The locations of the satellite tracks used in this study are shown in Figure 1 along with their GEOS-3 orbit number. The data was selected from the Pacific Ocean to avoid the complications of isolated volcanic centers. (Analyses of such areas will be undertaken when more complete data coverage is available). Because of the limited current coverage, emphasis thus far has been placed upon analysing tracks oriented as closely as possible to perpendicular to the direction of seafloor spreading. The available tracks entailed considerable compromise from ideal, however.

The geoid undulations are presented above the reduced seafloor bathymetry in Figure 2. Bathymetry for the North Pacific is from Chase et al. (1970), and for the South Pacific from Mammerickx et al. (1975). Depths have been corrected for sound velocity (Matthews, 1939) and for sediment loading (Ewing et al., 1968; Ewing et al., 1969). Isochron locations used to calculate residual depths (not shown) are taken from Heron (1972), Larson and Chase (1972), Larson and Hilde (1975), and Hilde et al. (1976), and the empirical depth versus age relation is from Parsons and Sclater (1977).
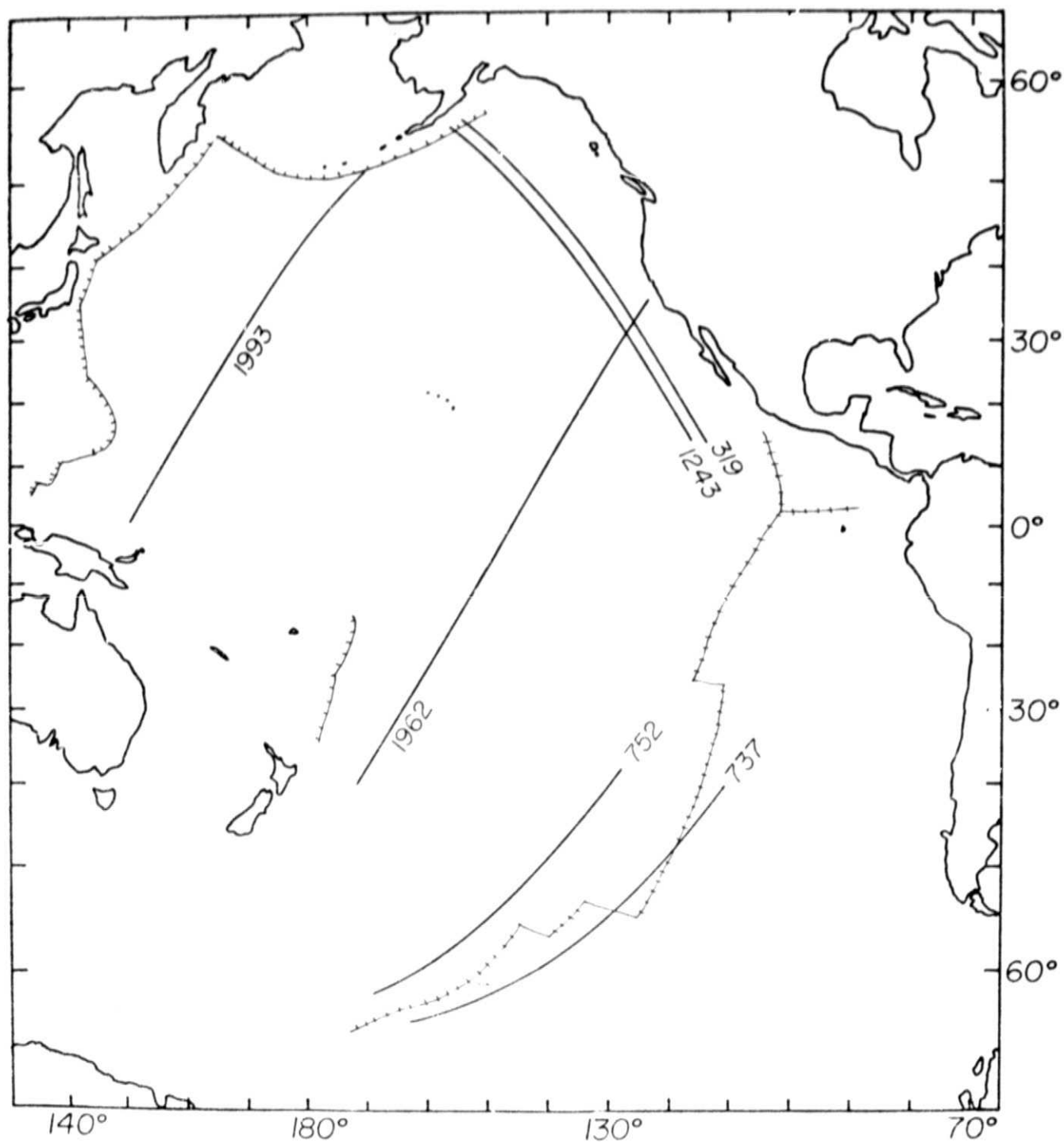
Figure 1.   Locations of altimetry tracks.   Ocean rises: ++++++;
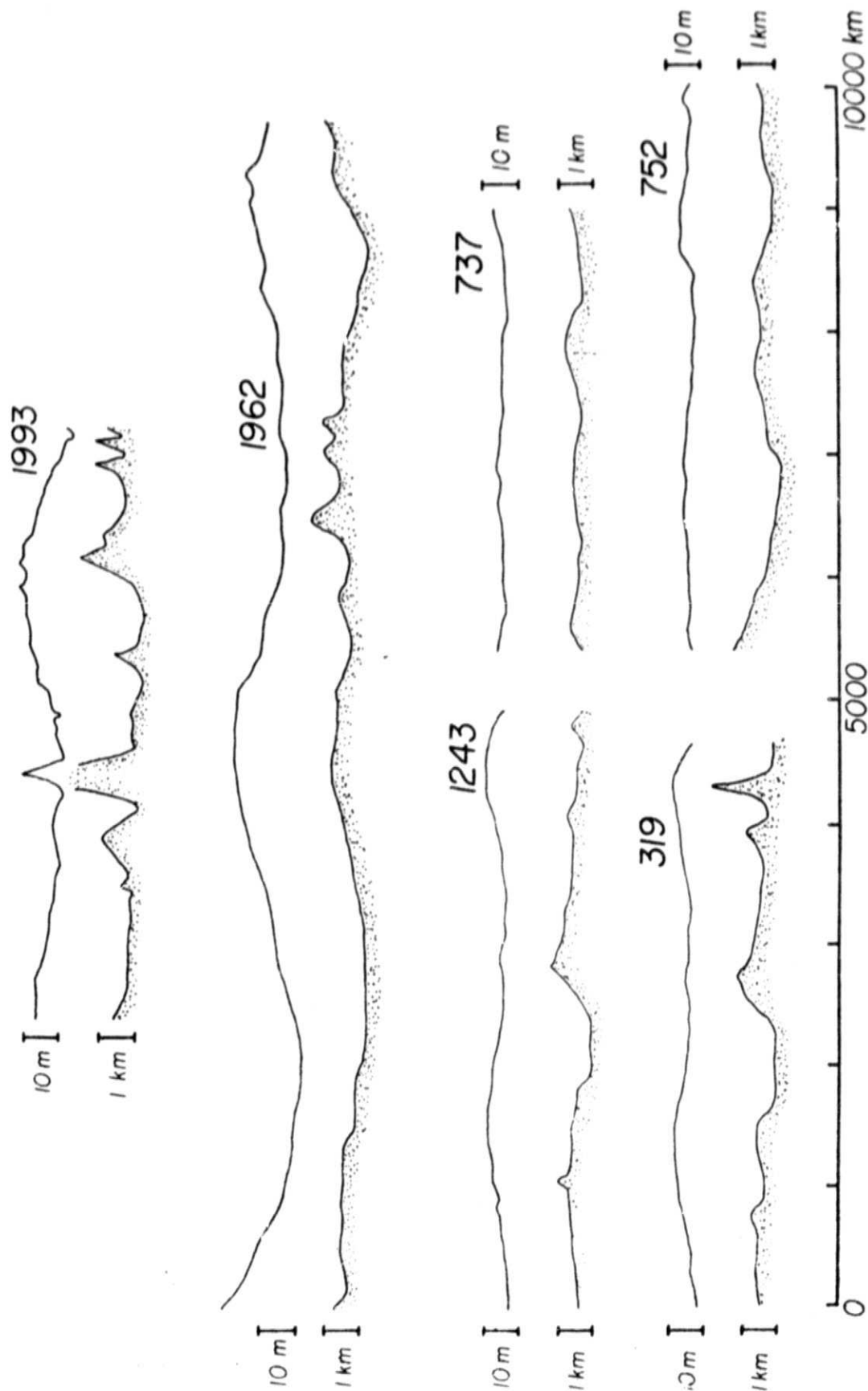   subduction zones: ||||||||| .

Figure 2. Smoothed versions of the geoid (upper) and reduced topography (lower) for each track. Both are detrended by a second degree polynomial. The sea-floor topography has been corrected for sediment loading where possible.

Before any admittance analysis is undertaken, it is worth examining the qualitative correlation of the geoid with either the bathymetry or the residual depth. The profiles in Figure 2 reemphasize the results of Cochran and Talwani (1977): the intermediate wavelength geoid (200-1000 km) shows reasonable correlation with most of the volcanic features, but the longer wavelength geoid (greater than 1000-2000 km) shows only slight correlation with the topography (Figure 2). No improvement is realized in the visual correlation at long wavelengths by additional smoothing of the profiles.

Strong positive correlations between geoid and topography can be seen where track 1993 crosses several seamounts near the Chinook Fracture Zone and where it intersects the Emperor Seamounts. A positive correlation is also noted where track 1962 crosses the Line Island Ridge (at about 4500 km); almost no geoid anomaly exists where the track crosses the Cook Islands implying more local compensation. The tracks over the youngest lithosphere (737 and 752) exhibit only low amplitude and long wavelength geoid anomalies as do tracks 1243 and 319 also over young lithosphere. Except for track 752 which showns a strong negative correlation between topography and geoid, the topography over this young lithosphere appears to be compensated at shallow depths. Some evidence for a negative correlation at long wavelengths is also observed in tracks 1993 and 1962 away from the volcanic features. The evidence is not definitive, however.

2.3 Application of Admittance Analysis

2.3.1 Isolated Track Analysis

The geoid height and bathymetry profiles were Fourier transformed, and admittances (eq. 4) and coherences (eq. 5) calculated for each satellite track using a band-averaged cross-spectral technique. The results are shown in Figure 3, with the complex component translated into phase. For the band-averaging used ($Q = 0.25$) and 95% significance level the co-herence is about 0.6. As can easily be seen, few of the coherences between geoid and topography exceed this value indicating that less than 33% of the energy is coherent between the two profiles. The overall lack of coherence between the geoid and topography is further accentuated by the large scatter in phases. Simple causative relations between the two would result in either a 0° or 180° phase. Calculation of the ad-mittance between geoid and residual depth produces comparable or lower coherences and equally poor phases. The amplitude of the admittance is indistinguishable from those calculated from the corrected bathymetry. This is largely because all the tracks have been detrended before processing using a second order polynomial. The second order polynomial removes most of the longest wavelength variations associated with the age dependence. It should also be noted that most of the tracks are nearly parallel to the isochrons. It is interesting to note that the coherences that are equal to or greater than 0.6 are
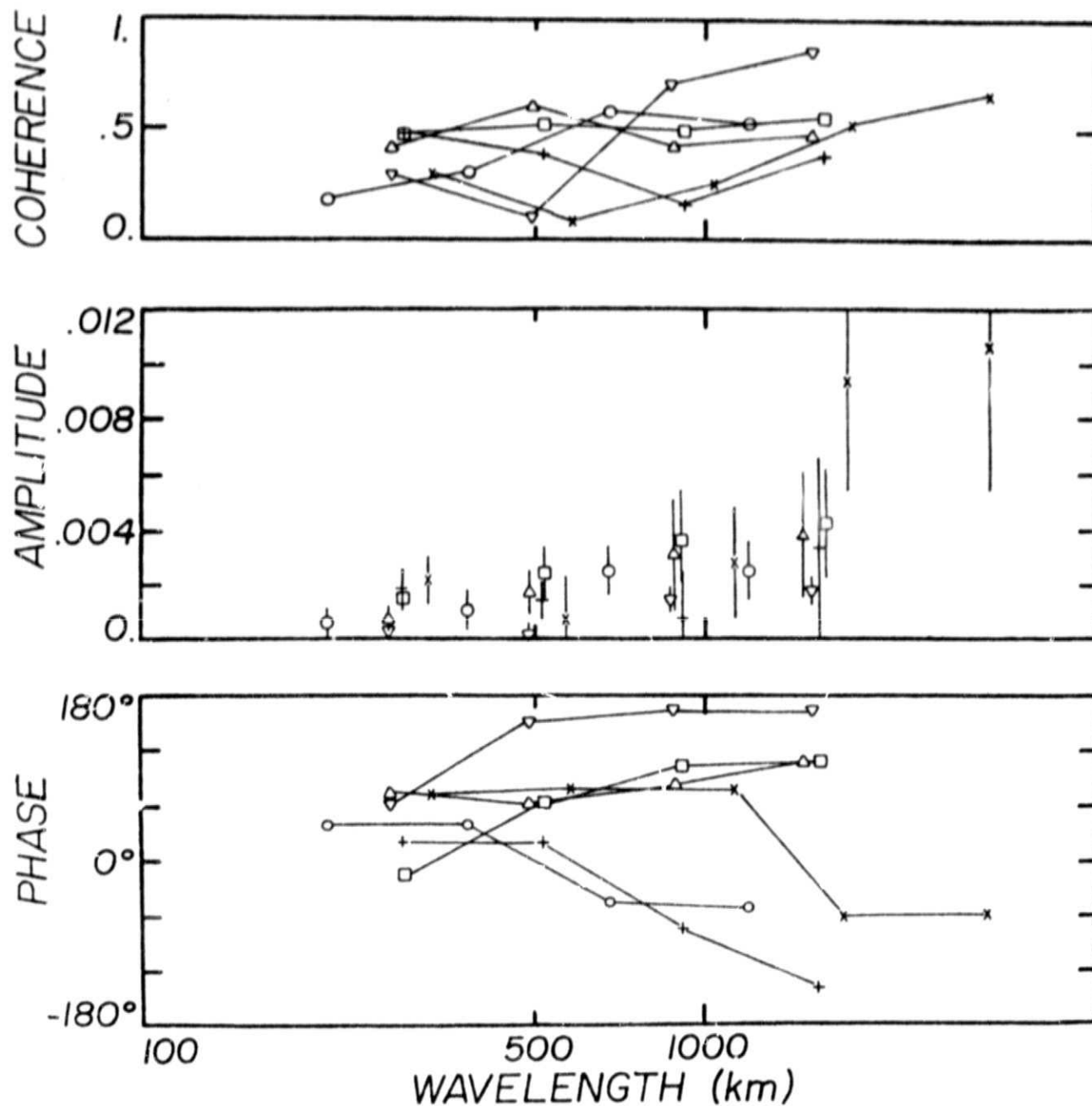
Figure 3.   Results of the spectral analysis. The 95% significance level
             for the coherences is approximately 0.6. The error bars on
             the amplitudes represent one standard deviation. No error
             bars are shown for the phases because at these low coherences
             one standard deviation is nearly ±180°. Not that there is
             usually a large change in phase between the wavelengths of 500
             and 1000 km.   (+) 1993; (x) 1962; (Δ) 319; (□) 1243; (o) 737;
             (∇) 752.

usually for wavelengths greater than 1000 km (see tracks 1962 and 752). The high coherence for track 1962 may result from the dominance of the Line Island Ridge in the profile; no volcanic features stand out on track 752. The significance of this result is again somewhat diminished by the scatter in the phases.

In an effort to obtain more statistically significant admittances, the results from the three oldest tracks, 1993, 1962 and 2488 have been combined. The results are shown in Figure 4. The averaging has apparently caused little change in the admittances. The coherences are still statistically insignificant for wavelengths smaller than 1000 km; however, the coherences for wavelengths greater than 1000 km have now become more noteworthy because the 95% significance level has dropped to 0.42. If the low coherences found were simply the result of a high noise level, increasing the number of samples by averaging should improve the coherence. The lack of improvement may imply that the physical mechanism responsible for the geoidal undulations of 300-1000 km wavelength are truly unrelated, or at least only weakly related, to seafloor topography. The non-zero phases also appear to be unchanged by the averaging and do not manifest the instability often associated with high noise levels. A phase reversal may still be surmised from the rapid change of phase near 1000 km wavelength.

Of the three parameters calculated, the phase is by far the most uncertain. Error bars at the 95% confidence level span the entire 360° cycle and are thus not shown. The phase is most sensitive to the details of the bathymetry and the sediment corrections. In areas such as the South Pacific, it is not known how accurate the bathymetry and isopachs are, even at long wavelengths. Poor phase estimates are also found in the NE Pacific where both are well known suggesting that the origin of the phase uncertainties should be sought elsewhere. One advantage of shipboard gravity measurements is that the bathymetry can be concurrently measured; however, the short wavelength features dominate the signal. With these points in mind, it is difficult to place even a positive or negative sign on the admittance at long wavelengths. However, the trend in most of the phase curves suggests that there may be a phase reversal somewhere between the wavelengths of 500-1000 km.

2.3.2 Discussion

The low coherences and small admittances at intermediate wavelengths (200-1000 km) support the conclusion that the intermediate wavelength topography may be compensated at shallow depth (Figure 4). In fact, both this study's results and those of McKenzie and Bowin (1976) might be explained by compensation in a layer of varying thickness (Airy compensation). McKenzie

and Bowin rejected this model because the average thickness of
this layer must be much thicker than the oceanic crust. If
this Airy compensation model accounted for all the observations,
a much higher coherence would be expected and the admittance
should be real.

The model favored by McKenzie and Bowin was their plate
model. In this model the intermediate and long wavelength
topography is compensated by bending an elastic plate of total
thickness 2h (solid lines in Figure 4); the short wavelength
topography is not compensated. The plate model reproduces
the observations with wavelengths less than 1000 km rather well
if the plate half-thickness (h) is taken to be 5-10 km and the
shear modulus between 10^{10} and 10^{11} Nm^{-2}. Again, however, the
consistently low coherences argue against an admittance wholly
determined by the plate model.

The above models require a high coherence between geoid and
topography because the source of both lies within the litho-
sphere. The low coherences might indicate that the source of
the geoid undulations lie below the lithosphere. The gravity
anomalies and deformations arising from convective processes
result in a real or zero admittance (McKenzie, 1977). The zero
admittance is the result if large viscosity variations completely
decouple the convective stresses from the overlying plate. The
decoupling effectively reduces or eliminates the coherent surface
deformation. This appears to be the case best represented by
the data. Not enough data currently exists to put rigorous
bounds on the nature of the decoupling zone, however.

McKenzie (1977; Appendix C) gives admittances for convection
partially decoupled from the lithosphere by a low-viscosity zone
of thickness d. The admittance depends upon the thickness of
the layer (d) and the viscosity contrast between the convecting
region and the low-viscosity layer. The thickness of the low-
viscosity layer is determined from the wavelength at which the
admittance changes phase (1000 km for the averaged data in
Figure 4) and the viscosity contrast by both the range of wave-
lengths over which the admittance remains negative and by the
largest negative amplitude. Unfortunately, we have little
control over the viscosity contrast due to the lack of longer
wavelength data, but the thickness of the low-viscosity layer
is estimated to be 200-300 km. There is no resolvable age
dependence, although the profiles over younger lithosphere
change phase at shorter wavelengths.

Kaula's (1977) statistical analysis of gravity and topo-
graphy over oceanic regions agrees well with the results pre-
sented here. Similar negative admittances are implied for
wavelengths shorter than 5000 km. (Kaula's analysis only
included harmonic degrees as high as 36, so no lower limit can

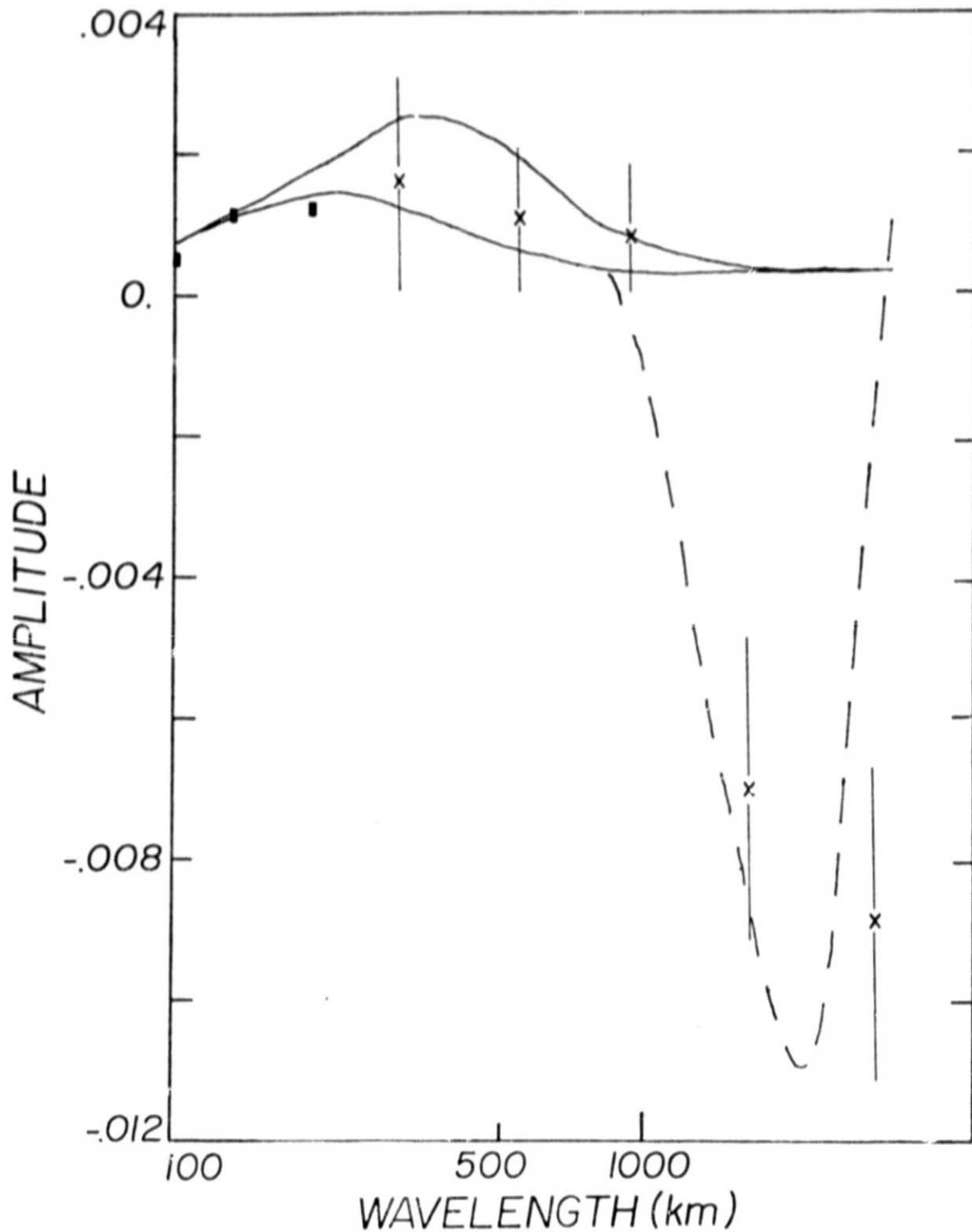Figure 4. Several models are superimposed on the averaged admittances. Short wavelength admittances from McKenzie and Bowin (1976) are shown as solid rectangles. The solid curves are from the plate model; the upper curve is for h = 10 km and the lower is for h = 5 km. All other parameters are as in McKenzie and Bowin. The dashed curve is the decoupling model of McKenzie (1977) for M = 100 and d = 200 km.

be estimated.) However, combining this 5000 km upper limit
with the lower limit of 1000 km from this study suggests a
viscosity contrast of about 100 between the asthenosphere
and the mantle below.

A decoupling model also admits an explanation for the non-
real admittances. Even though the convective stresses create
negligible seafloor topography, topography can result from
thermal expansion. Since the lithospheric plate may move re-
lative to the convecting mantle, the finite thermal conductivity
of the lithosphere will cause any topography created by thermal
expansion to be out of phase with respect to the mantle heat
sources responsible for the geoidal undulations. If this is
the case, some estimate of the relative motion between the
lithosphere and convecting mantle might be obtained by studying
the phase differences between geoid and gravity and topography.

It is not entirely clear whether a single physical process
correctly describes the data. For instance, the longer wave-
lengths (greater than 1000 km) may be controlled by the con-
vection and the viscous decoupling, but the intermediate wave-
lengths may result from compensation of inhomogeneities within
the plate through a plate model (McKenzie and Bowin, 1976) or
Airy model. The intermediate wavelength admittances do fit a
plate model within reason. Or, both processes may simultaneously
occur.

Further speculations on the origin of the geoid and sea-
floor topography must await more comprehensive data. Thus far
only two-dimensional admittance have been studied and not neces-
sarily in the optimum orientations nor over a suitable spread of
wavelengths. Consideration of the geoid over a large oceanic
area will better enable us to relate the long wavelength geoid
to the regional tectonics and to appreciate the contribution
of "isolated" volcanic features to the regional geoid. Admit-
tances from three-dimensional convective systems may result in
totally new interpretations.

2.3.3 Areal Admittances over the Hawaiian Swell

To further investigate the relationship between geoid
and seafloor topography two-dimensional admittances were
calculated for the area shown in Figure 5. Admittances band-
averaged according to wave number were nearly identical to
those found in the track analysis. The coherences were also
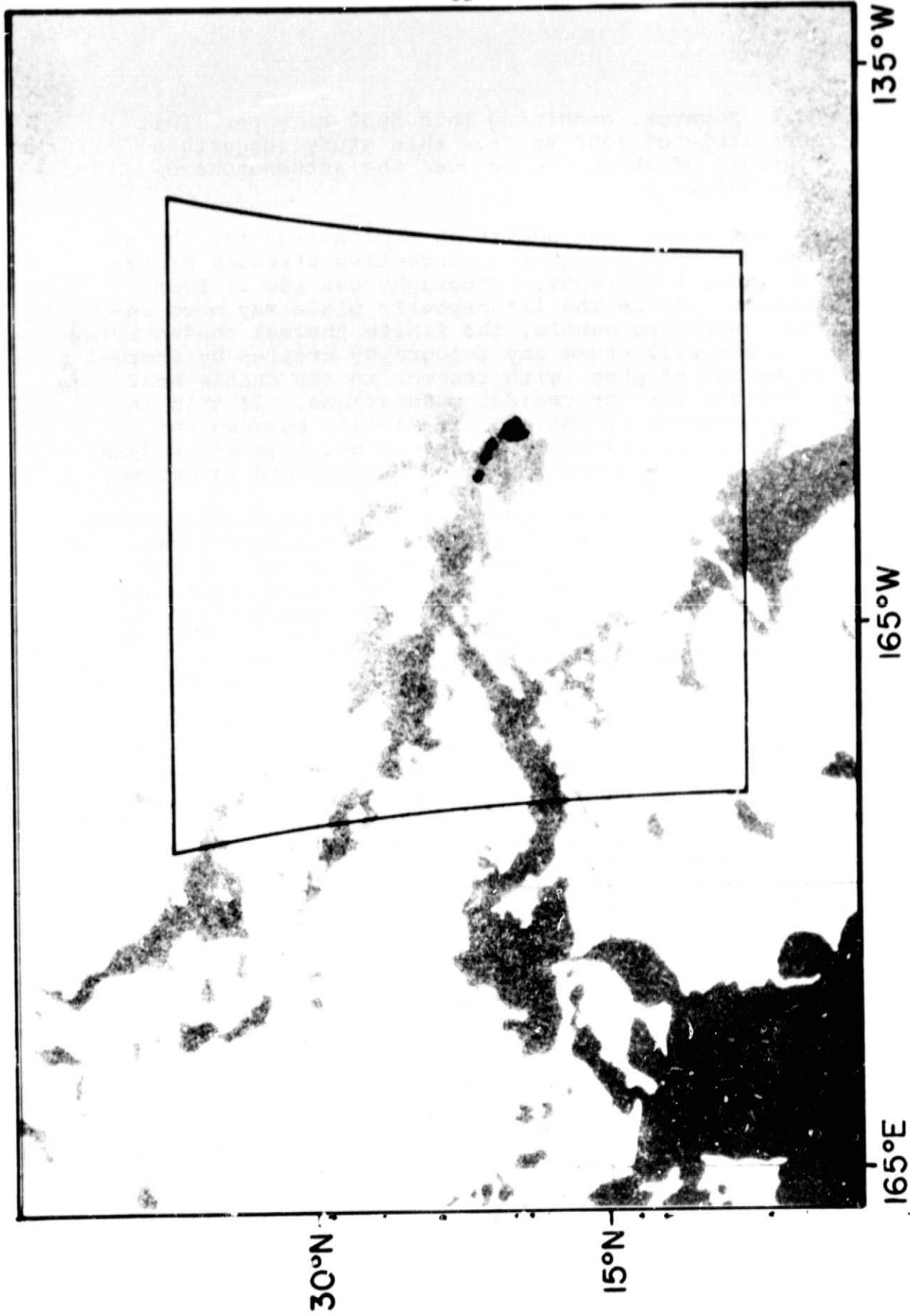found to be similarly low.

Figure 5. Study area. Grey depths <4570 m. Black above sea level.

Directional band-averaging, however, resulted in anisotropic admittances and coherences. Admittances crossing east-west striking structures (from north-south profiles) were smaller but more coherent than those from east-west profiles. Since the geological structures in this area predominantly strike east-west, this is further evidence for a coherent geoid only ov.r volcanic structures. Unfortunately, the area considered for analysis was too small to provide good estimates of the long wavelength admittances.

2.3.4 Global Statistical Analyses

Covariance analyses can also be carried out on a sphere:

$$C(gb, \tau) = \frac{1}{8\Pi^2} \int_T \int_0^{2\Pi} g(r)b(\tau)\,dA\,dr, \tag{2.6}$$

where dr is an element of area on a unit sphere of total surface, T, A is azimuth, and τ is arc distance, and Legendre polynomial transforms (analogous to Fourier transforms) applied to obtain a power spectrum:

$$\sigma_\ell^2(gb) = \frac{\sqrt{2\ell+1}}{2} \int_0^\Pi \bar{P}_{\ell 0}(\cos \tau)C(gb, \tau)\sin\tau\,d\tau, \tag{2.7}$$

where ℓ is spherical harmonic degree and $\bar{P}_{\ell 0}$ is the zonal harmonic normalized to mean square unity. The estimated admittance is then

$$Z_\ell = \sigma_\ell^2(gb)/\sigma_\ell^2(bb). \tag{2.8}$$

Such analyses were applied to global data sets of $5^\circ \times 5^\circ$ means of gravity anomalies based on the NASA-Goddard SFC GEM-6 solution (Smith et al., 1976) plus DoD $1^\circ \times 1^\circ$ means, and of topography compiled by Lee (Balmino et al., 1973). These data sets were divided into 15 terrain types. Also included in he analysis were plate velocities and boundary types. The details are described in Kaula (1977). Given here are the results for the combination of oceanic terrain types.

Harmonic Degree(s) ℓ	Auto Degree Variances		Cross Degree Variance	Admittance
	Gravity $g.g$ $mgal^2$	Topography $b.b$ km^2	$g.b$ $mgal.km$	g/b $mgal\ m^{-1}$
0	-1.	-0.002	-0.00	
1	2.	0.056	0.23	0.004
2	39.	0.114	-1.65	-0.014
3	39.	0.074	0.60	0.008
4	14.	0.066	0.66	0.010
5	18.	0.039	0.42	0.011
6	19.	0.034	0.56	0.016
<7-9>	7.	0.024	0.07	0.003
<10-12>	5.	0.017	-0.03	-0.002
<13-15>	6.	0.014	0.13	0.009
<16-18>	2.	0.012	0.01	0.001
<19-24>	1.3	0.004	-0.01	-0.002
<25-36>	1.7	0.007	0.00	0.000
Sums	219.	0.69	1.32	

The low admittances in the 7-36 degree range--corresponding to wavelengths of 6000 down to 1100 km--are consistent with the findings from the altimetry profiles described above. The larger positive admittances at 3 to 6 are evidently the consequence of seafloor spreading, which trend has been removed from the track data discussed above or by McKenzie & Bowin (1976). The sign reversal between degrees 2 and 3 mimics what McKenzie (1977, Fig. 6a) predicts for a 3000 km deep convecting layer of non-deformable lower boundary, but this seems too vertiginous a leap between model and data to take seriously.

It is planned to redo the global covariance analyses utilizing some improvements in technique (Kaula, 1978).

3. LITHOSPHERIC THINNING

In this study we will analyze a region in the Central Pacific containing a large portion of the Hawaiian chain. Our aim will be to show that the major portion of the Hawaiian swell is caused by a local thinning of a higher density lithosphere on top of a lower density asthenosphere. To accomplish this, the relationship between geoid heights and seafloor topography will quantitatively be analyzed at intermediate wavelengths ($300 < \lambda < 3000$ km). Cochran and Talwani (1977) used gravity data to qualitatively determine this relationship over many oceanic areas. They found that there is generally a poor correlation except over active spreading zones or mid-plate volcanic areas. A positive correlation between free air gravity and topography
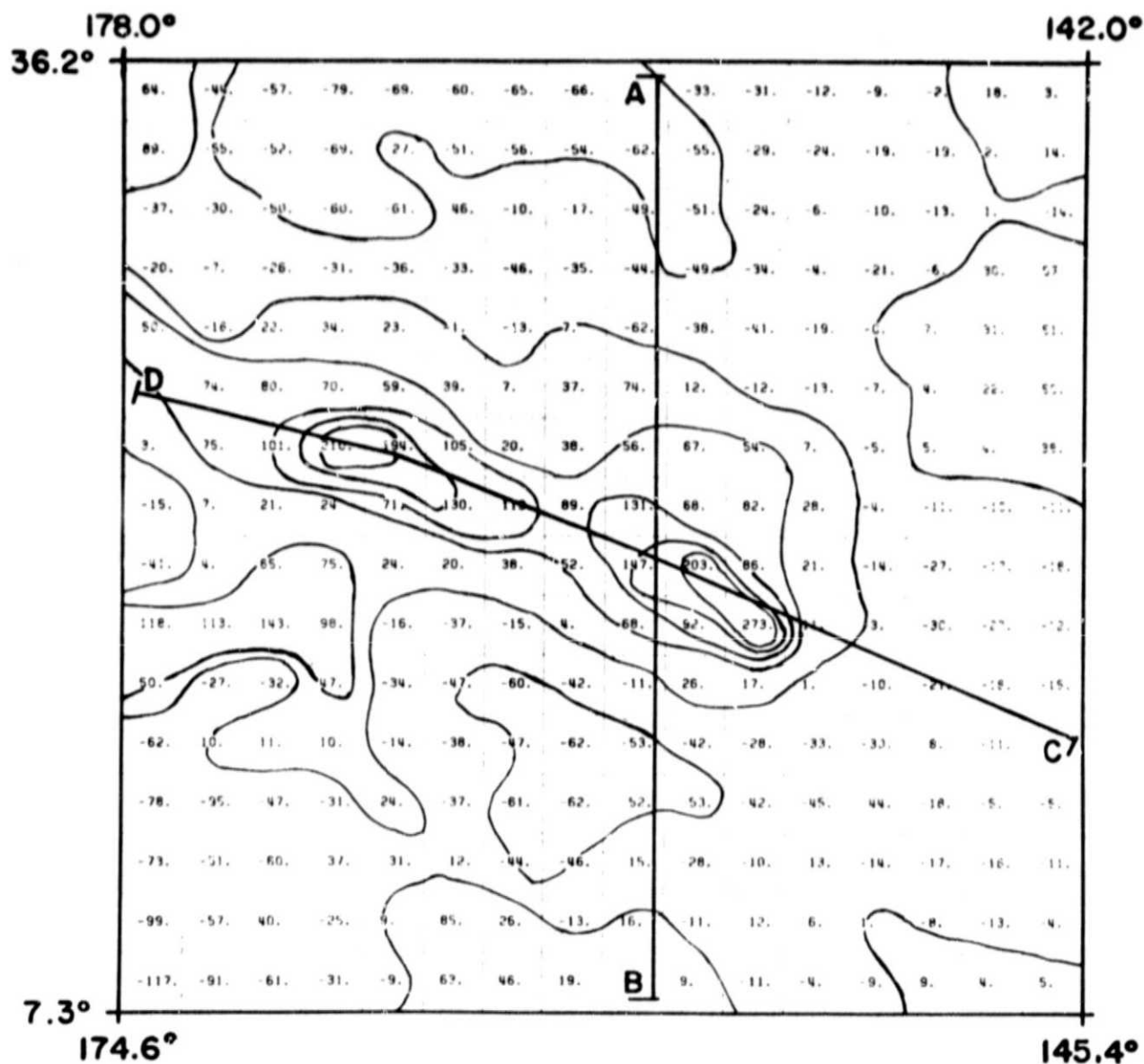
178.0°   142.0°

36.2°

64.	-44.	-57.	-79.	-69.	60.	-65.	-66.	**A**	-33.	-31.	-12.	-9.	-2.	18.	3.
89.	55.	-52.	-69.	27.	-51.	-56.	-54.	-62.	-55.	-29.	-24.	-19.	-19.	2.	14.
-37.	-30.	-50.	-60.	-61.	46.	-10.	-17.	-49.	-51.	-24.	6.	-10.	-19.	1.	-14.
-20.	-7.	-26.	-31.	-36.	-33.	-46.	-35.	-44.	-49.	-34.	-4.	-21.	-6.	36.	57.
50.	-16.	22.	34.	23.	1.	-13.	-7.	-62.	-38.	-41.	-19.	-0.	7.	31.	51.
D 74.	80.	70.	59.	39.	7.	37.	74.	12.	-12.	-13.	-7.	4.	22.	55.
3.	75.	101.	210.	194.	105.	20.	38.	56.	67.	54.	7.	-5.	5.	4.	39.
-15.	7.	21.	24.	71.	130.	116.	89.	131.	68.	82.	28.	-4.	-11.	-15.	-11.
-41.	4.	65.	75.	24.	20.	38.	52.	147.	203.	86.	21.	-14.	-27.	-17.	-18.
118.	113.	143.	98.	-16.	-37.	-15.	4.	-68.	52.	273.	74.	3.	-30.	-27.	-2.
50.	-27.	-32.	47.	-34.	-47.	-60.	-42.	-11.	26.	17.	1.	-10.	-27.	-18.	-15.
-62.	10.	11.	10.	-14.	-38.	-47.	-62.	-53.	-42.	-28.	-33.	-33.	8.	-11.	**C**
-78.	-95.	47.	-31.	24.	-37.	-81.	-62.	52.	53.	42.	-45.	44.	18.	-5.	-5.
-73.	-51.	-60.	37.	31.	12.	-44.	-46.	15.	28.	-10.	13.	-14.	-17.	-18.	11.
-99.	-57.	40.	-25.	4.	85.	26.	-13.	16.	11.	12.	6.	1.	-8.	-13.	-4.
-117.	-91.	-61.	-31.	-9.	63.	46.	19.	**B**	9.	-11.	-4.	-9.	9.	4.	5.

7.3°

174.6°   145.4°

Figure 6. Seafloor topography averaged into areas 203 km on a side with best fitting plane removed. Units are decameters.

or geoid height and topography can be produced by three
mechanisms: support of topography by stresses within the
lithosphere, dynamic support at the base of the lithosphere,
undulating lithosphere/asthenosphere boundary. McKenzie (1967)
has shown that the first possibility can be discounted for
wavelengths greater than 1000 km. Cochran and Talwani (1977)
have attributed the correlation associated with spreading
ridges to cooling and subsidence of the lithosphere as it
moves away from the ridge crest. We feel that this thermal
mechanism also produces the observed correlation over the
Hawaiian chain.

In the first part of the analysis we will determine that
part of the ocean geoid which is coherent and in phase with
the topography. A local compensation mechanism will then be
proposed to reproduce this part of the geoid. Out of the many
possible local compensation mechanisms only Airy-Heiskanen
compensation using two compensation depths will be investigated.
Short wavelength topography will be compensated within the upper
part of the lithosphere and longer wavelengths will be compen-
sated at the lithosphere/asthenosphere boundary. This model
implies a variable thickness lithosphere. Since geoid heights
alone cannot distinguish between different compensation mechanisms,
we will try to justify our choice by showing that the variable
thickness lithosphere model can explain the subsidence of the
islands along the Hawaiian-Emperor chain.

Airy compensation for the Hawaiian swell requires that the
lithosphere beneath the swell be tens of kilometers thinner than
the surrounding lithosphere. As pointed out by Detrick and
Crough (1978) this thinning must occur over a time interval of
less than 5 my. The characteristic time for a heat perturbation
to conduct through 30 km of lithosphere is about 30 my. Unless
very large heat anomalies are introduced, the lithosphere cannot
be thinned fast enough by a purely conductive mechanism (Crough
and Thompson, 1976). A way to produce rapid thinning is to
advect heat to the base of the lithosphere and let the lithosphere/
asthenosphere boundary migrate in time. We propose a simple
one-dimensional heat flow model with a moving solid/liquid
phase boundary to account for both the rapid thinning and later
gradual thickening of the lithosphere along the Hawaiian chain.

3.1 Data

The region of interest is shown in Figure 5. The area
outlined is a 3248 km square enclosing much of the Hawaiian
swell. For analysis purposes the area is divided into 256
equal squares of 203 km on a side (approximately 2°x2°). Geoid
and bathymetric averages are estimated for each square. A
mean and best fitting plane are removed from both before a two
square cosine taper is added to the perimeter of the region.

Bathymetry. Seafloor bathymetry was taken from Chase et al. (1970) and was corrected for water velocity using Matthews tables (Matthews, 1939). No sediment corrections were applied to the data because the sedimentary cover is regionally uniform (Ewing et al., 1968) and the large averaging areas largely negate the influences of local accumulations. Figure 6 shows the results after averaging. The WNW striking island chain can clearly be seen. The deep and rise flanking the island chain do not show up after averaging because the box size is greater than the wavelength of these features. The Hawaiian swell shows up clearly with a strike similar to the island chain and a half-width of about 1000 km. The swell is elongated on the north but drops sharply to the south at the southeast end of the chain. The mean depth of the region (5169 m) fits the empirical depth-age curve at about 60 my; the magnetic age of the area is closer to 100 my.

Geoid. GEOS-3 altimeter data was averaged into the same squares as the bathymetry (Figure 7). The dominant feature in the geoid is the long wavelength high over the Hawaiian swell region with an amplitude of roughly 10 m. The central portion of this high has a feature elongated in the WNW direction. This feature probably reflects the part of the geoid produced by the island chain. The remainder of the high is roughly circular with a half-width of about 1200 km in the NS direction and about 1600 km in the EW direction. The peak-to-trough amplitude in the EW direction is about 12 m and in the NS direction is only 10 m.

Geoid data was used in this analysis for a number of reasons. First this data is best suited for studies at intermediate wavelengths. At the shorter wavelengths undulations contain very little power. At the longer wavelengths (angular order <10) the GEOS-3 derived geoid may contain inaccuracies due to satellite tracking errors. The second reason this data was used is because Watts (1976) has used surface gravity data to infer the lithospheric and upper mantle density structure over a region roughly the same as that shown in Figure 5. Since the GEOS-3 geoid and the surface gravity measurements are independent data sets, it is interesting to compare the results of the two analyses.

3.2 Airy Compensation Models

There are a number of isostatic compensation models one can use to calculate the geoid from the topography. Walcott (1969) used a flexure model to fit the observed gravity anomalies over the Hawaiian region up to 300 km away from the islands. The best fitting flexural parameter was found to be 110 km. This model of compensation is important at wavelengths near 100 km but is less important at longer wavelengths.

Other important compensation mechanisms include Pratt and Airy-Heiskanen compensation. For these types of compensation

178.0° 142.0°
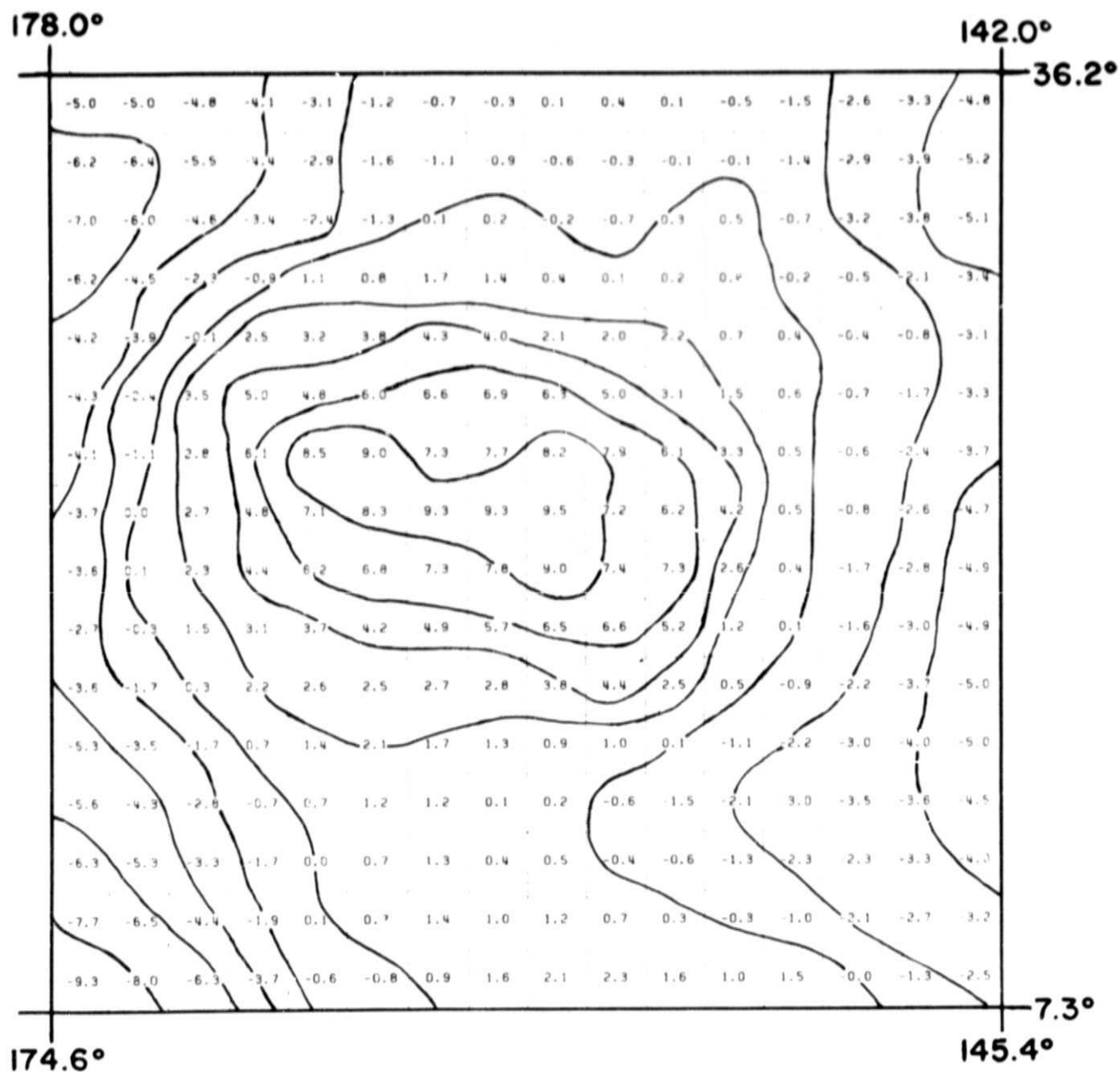36.2°

174.6° 145.4°
7.3°

Figure 7. Geoid heights averaged into areas 203 km on a side with best fitting plane removed (meters).

the mass in every vertical column is the same from the surface
to the depth of compensation. For the Pratt model this is ac-
complished by varying the density in adjacent columns.   The
Airy model uses a constant density layer of variable thickness.
Local compensation can be composed of any number of layers and
any combination of the Pratt and Airy models.

The geoid for both of these models can easily be calculated
using a method proposed by Parker (1972). Let z be positive
upward and place the origin at a depth z_0 below the sea surface.
z_0 is chosen so that the maximum undulation in the density
interface (i.e., seafloor topography) is minimized. As an
example, take the calculation of the geoid height N from un-
compensated seafloor topography $h(x,y)$. Let $F[]$ denote the
Fourier transform of the quantity in brackets. Let $\hat{k}$, ρ_c and
ρ_w be the wavevector, crustal density and sea water density
respectively.   Then,

$$F[N] = \frac{2\pi G(\rho_c - \rho_w)}{|\bar{g}|} \exp(-|\vec{k}|z_0) \sum_{n=1}^{\infty} \frac{|\vec{k}|^{n-2}}{n!} F[h^n(x,y)] \quad (3.1)$$

where $\bar{g}$ = mean acceleration of gravity.

These are the exact equations for N due to the seafloor
topography. The series converge as long as $(max(h^2(x,y)))^{1/2}/z_0 < 1$.
For our case this means the seafloor topography can not be
above the sea surface. The smaller the above ratio is made
the faster the series converges. For all of the models cal-
culated this ratio was less than 0.5. Convergence of the series
was more than adequate after summing six terms in the series.

The geoid height for an Airy model was calculated by super-
imposing several surfaces of density contrast at different
depths. Suppose $N_1(x,y)$ is the geoid anomaly due to the un-
compensated topography. Let ρ_1 be the density of the crust
and ρ_2 the density of the lithosphere. If z_1 is the mean
depth of compensation, then the Fourier transform of the geoid
height is given by

$$F[N] = F[N_1] + \frac{2\pi G}{|\bar{g}|}(\rho_2 - \rho_1)\exp(-|\bar{k}|z_1) \sum_{n=1}^{\infty} \frac{|\bar{k}|^{n-2}}{n!} F[\{\frac{\rho_w - \rho_1}{\rho_2 - \rho_1}h(x,y)\}^n]$$

$$(3.2)$$

This can be generalized to any number of layers with different
wavelengths of topography being compensated at different depths.

The model adopted to satisfy the geoid data is shown in
Figure 8. Short wavelength topography (less than 800 km wave-
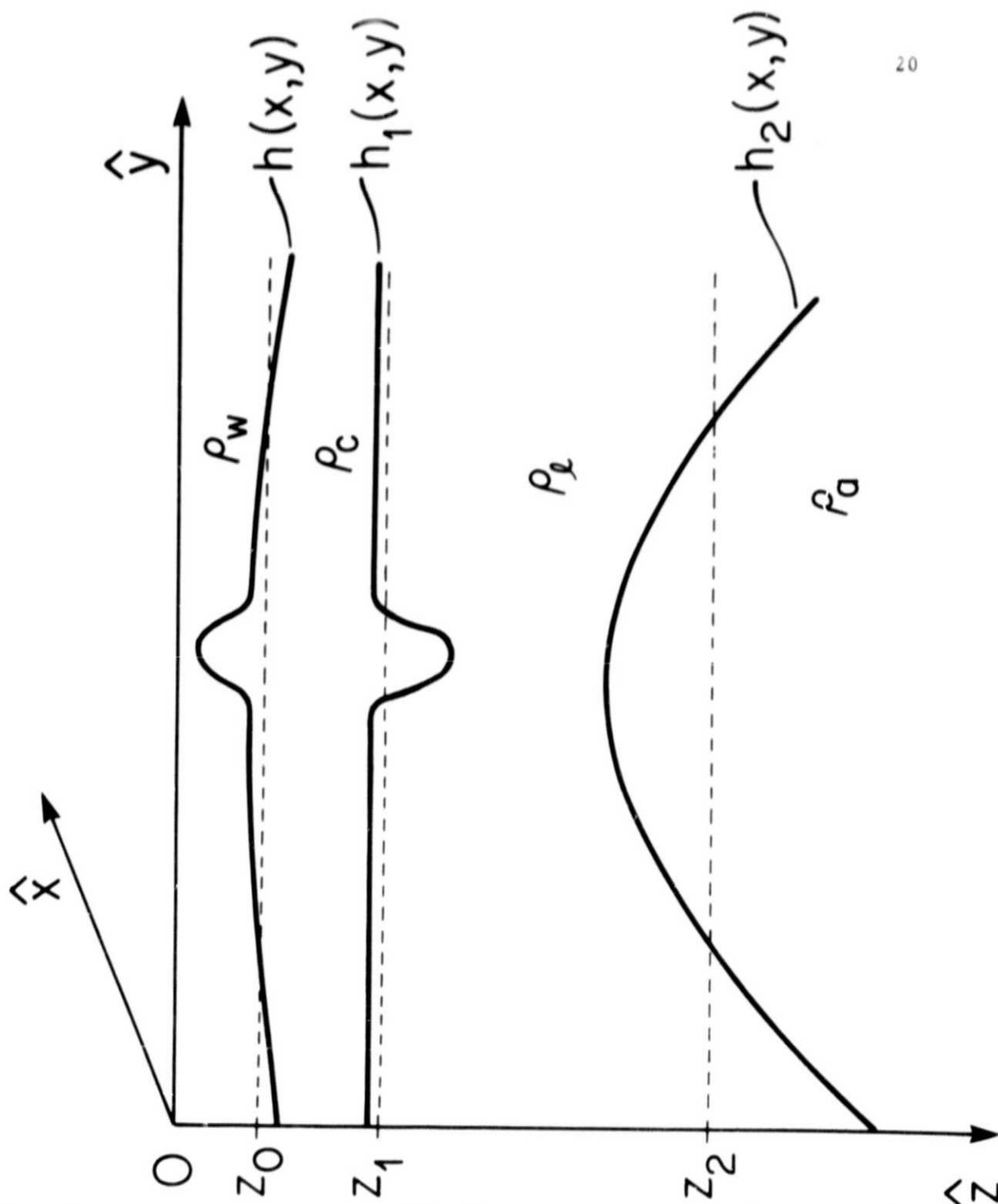length) is compensated at crustal depths while longer wavelength

Figure 8. Diagram of Airy isostatic model. $h(x,y)$, $h_1(x,y)$, and $h_2(x,y)$ are measured positive upward from z_0, z_1 and z_2 respectively. $h(x,y)$ is the seafloor topography. $h_1(x,y)$ and $h_2(x,y)$ are calculated from $h(x,y)$ is the wavelength domain.

$$h_1(\vec{k}) = H(|\vec{k}| - \frac{2\pi}{800})h(\vec{k})\frac{(\rho_w-\rho_c)}{(\rho_\ell-\rho_c)} , \qquad h_2(\vec{k}) = H(\frac{2\pi}{800} - |\vec{k}|)h(\vec{k})\frac{(\rho_w-\rho_L)}{(\rho_a-\rho_\ell)}$$

$H(\ )$ is the heavyside step function.

features are compensated at the lithosphere/asthenosphere boundary. The actual depth of compensation is most likely a much more complicated function of wavelength. A model with one depth of compensation is the simplest. This model was tested for a variety of compensation depths. These models fit poorly to the observed geoid at either the long or short wavelengths depending upon the depth of compensation. Because of this it was necessary to use a model with two depths of compensation. The crustal density (ρ_c) and mean thickness (z_1) were taken from Hussong (1972) and were not modelled. The only free parameters in the model were the mean depth of compensation for the long wavelength topography (z_2) and the lithosphere/ asthenosphere density contrast ($\rho_\ell - \rho_a$).

Before discussing the results of the modelling it is worthwhile commenting upon what exactly it is that the models are to match. An Airy model requires that the geoid be nearly coherent and in phase with the topography. It is therefore unreasonable to expect any model to account for all of the observed geoid. In order to determine what portion of the geoid can be modelled, the geoid was separated into two parts: one coherent and in phase with the topography, and one incoherent or out-of-phase with the topography. This separation was accomplished by calculating the band-averaged two-dimensional transfer functions between the topography and geoid. The coherent and in phase part of the geoid is reconstructed from the topography and the real part of the transfer functions. It should be noticed that the part of the geoid that is incoherent or out-of-phase with the topography (Figure 9) accounts for about 60% of the total energy. The rms residual from no model can be smaller than the rms standard deviation (2.71 m) of this part of the geoid.

A comparison of figures 7 and 9 reveals that there is a large portion of the Hawaiian geoid anomaly that is not reflected in the topography. It is important that this unrelated part of the geoid not be included in any regression of geoid and topography. Regression slopes obtained without removing this incoherent geoid will be strongly biased and will indicate deeper compensation depths.

The best fitting models found have mean depths of compensation between 50 and 90 km. This range and the best fitting model were determined by two methods. First we subtracted the model from the observed geoid and calculated a rms deviation. Taking the depth of compensation at 10,000 km (uncompensated model) we found an rms deviation of 12.9 m. Figure 10 shows this model. It looks very similar to the averaged seafloor topography (Figure 6). By comparing this model to the observed geoid (Figure 7) one can see that the amplitudes are much too large. The best fitting compensated model found by this method has a z_2 of 70 km and an rms deviation of 3.04 m. Figure 11
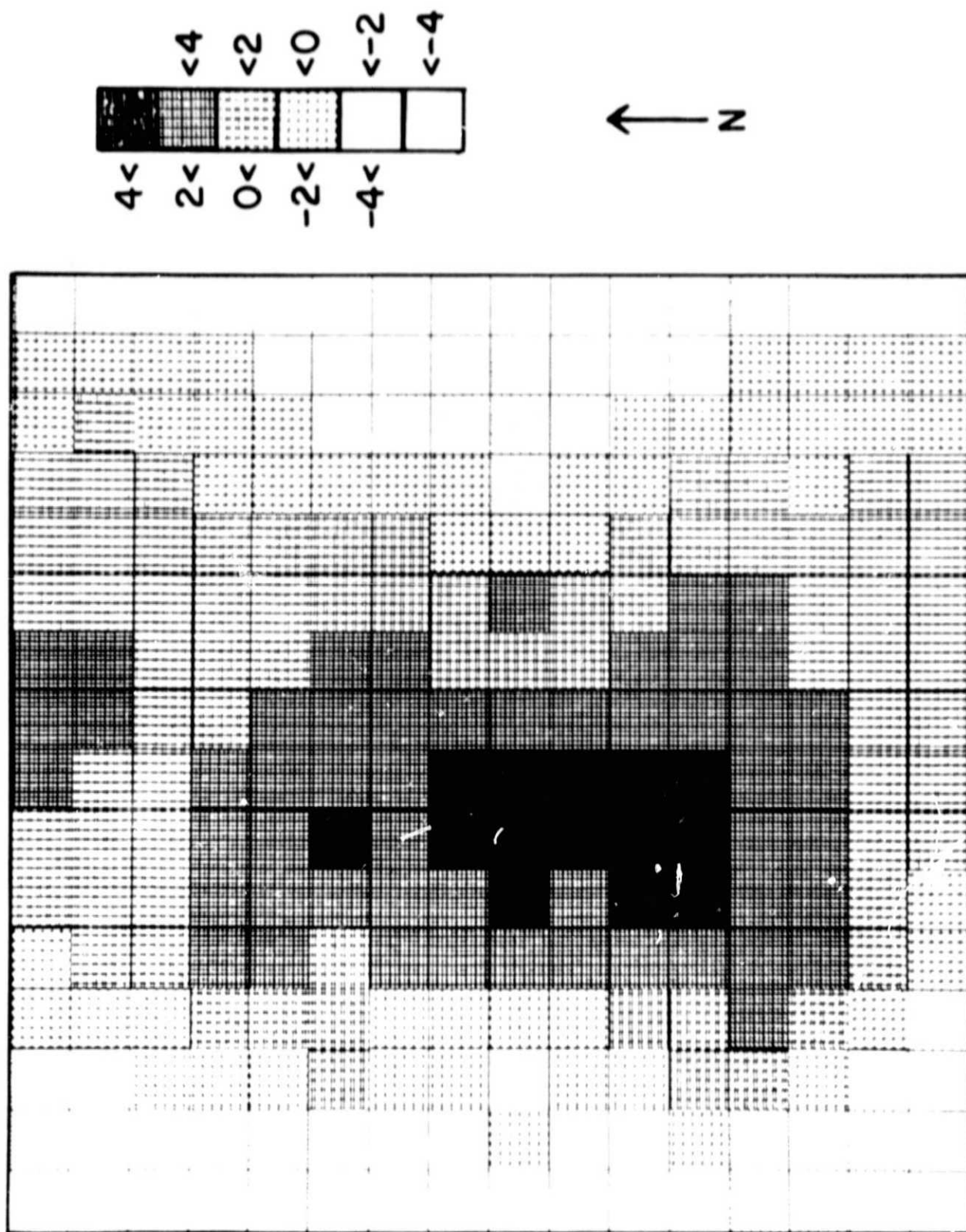
Figure 9. The part of the observed geoid height that is incoherent or out of phase with the topography. Units are in meters. This part of the geoid is dominated by a long wavelength undulation in the EW direction ($\lambda \approx 3200$ km).
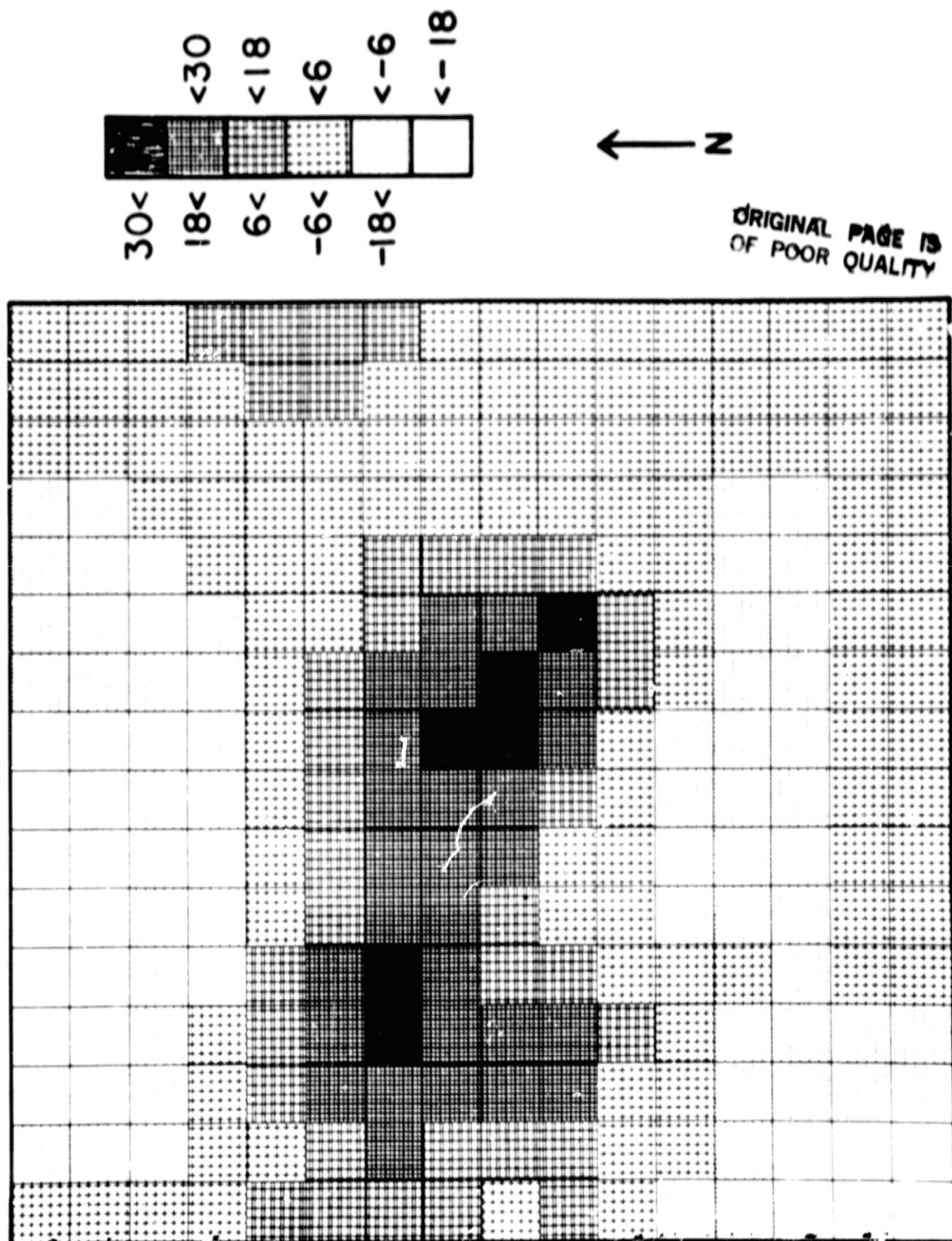
Figure 10. Geoid height calculated from uncompensated seafloor topography with density of 2.87 gm/cm³. Units are in meters.

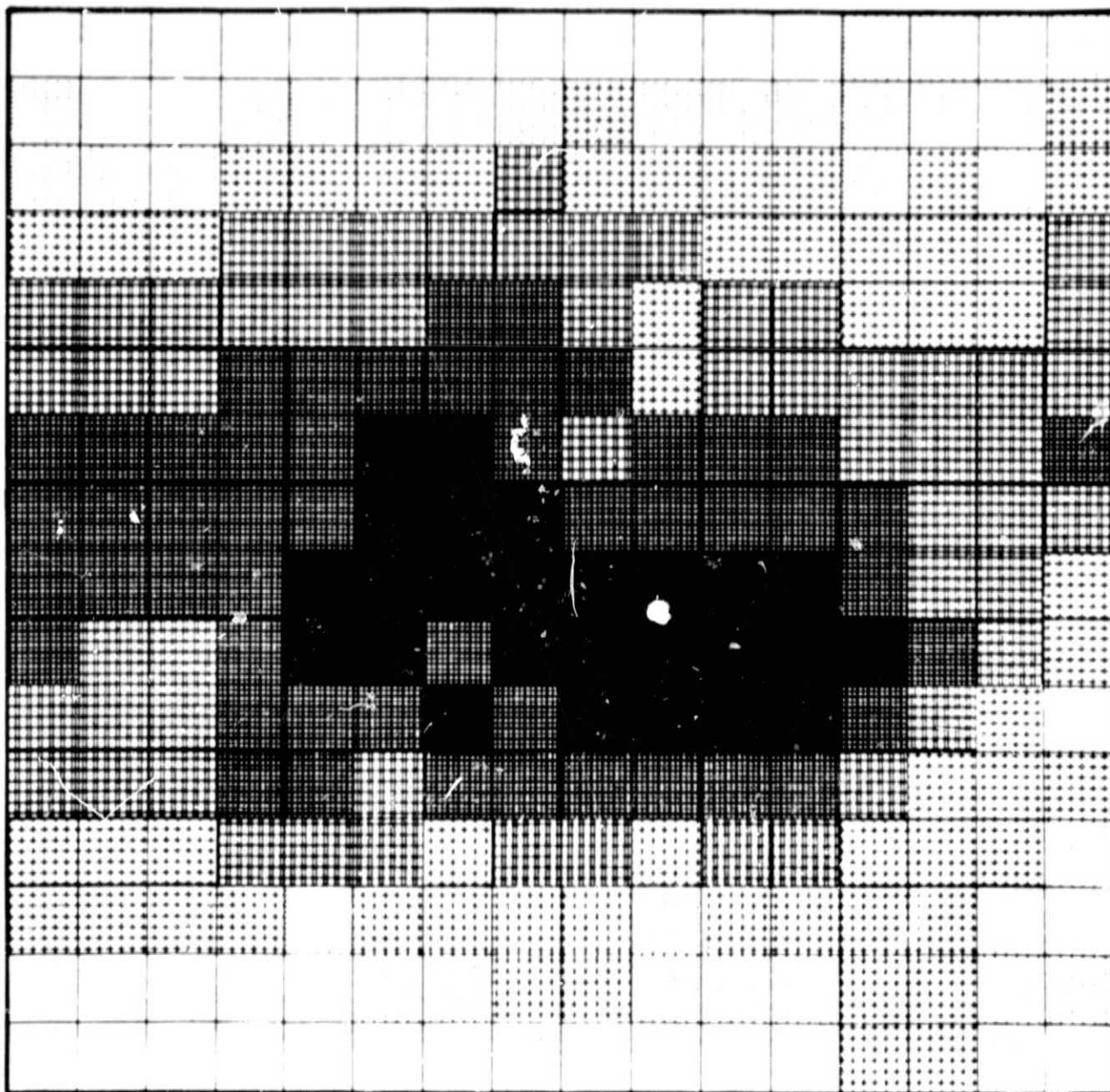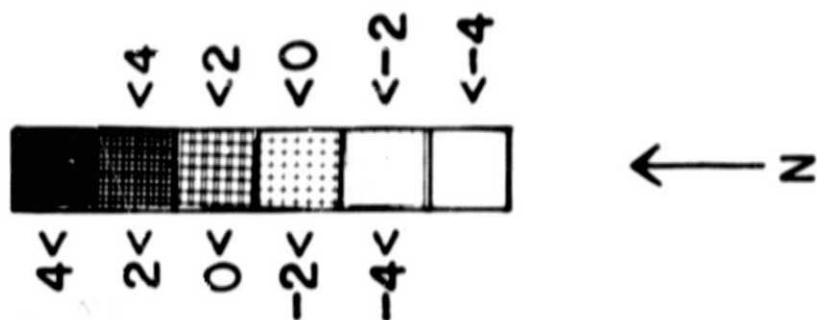Figure 11. Observed geoid minus geoid calculated from Airy model with $z_2 = 70$ km. There is a good visual similarity between this residual geoid and the incoherent and out-of-phase geoid. The rms deviation between them is 1.27 m.

shows the observed geoid minus the model for $z_2 = 70$ km.
Using this method we could not determine a range for the depth
of compensation because the incoherent and out-of-phase part
of the observed geoid produced a major part of the rms deviation.
By fitting models to the in phase and coherent part of the
geoid limits could be part on z_2. Again, a best fitting model
with $z_2 = 70$ km was found with an rms deviation of 1.27 m.
Depths of compensation of 50 and 90 km have rms residuals of
1.45 and 1.48 m respectively. The Table shows the rms deviation
between, the model and observed geoid, and model and the coherent
and in phase geoid, for a number of compensation depths.

Depth (km)	Observed Geoid -Airy Model, Meters	Coherent and in Phase Geoid -Airy Model, Meters
50	3.12	1.45
70	3.04	1.27
90	3.10	1.48
110	3.17	2.43
130	3.48	
10^5	12.97	

The density contrast $(\rho_\ell - \rho_a)$ is the parameter that determines
the amplitude of the undulations of the lithosphere/asthenosphere
boundary needed to support the surface topography. Models with
density contrasts of 0.06 to 0.12 gm/cm^3 produced nearly identical
geoids. Because of this insensitivity, it was not possible to
place definitive bounds on the density contrast. A lower bound
might be estimated by considering the maximum thinning possible.
The Airy model predicts that the lithosphere/asthenosphere
boundary will intersect the crust/lithosphere boundary if the
density contrast is less than 0.06 gm/cm^3. A density contrast
of 0.1 gm/cm^3 gives a more reasonable maximum thinning of 35 km.
This density contrast produces a lithospheric thickness beneath
the swell corresponding to a thermal age of about 35 my (Parsons
and Sclater, 1977). Figure 12 shows the two compensation
boundaries for tracks along and perpendicular to the island
chain for a density contrast of 0.1 gm/cm^3. The location of
these tracks are indicated on Figure 6. The thickening is ob-
served after the volcanically active islands are passed. The
maximum thinning does not appear to take place directly under
Hawaii but slightly to the west of it.

3.3 Thermal Model

The empirical depth/age and heat/flow age relations can
be fit by a thermal spreading model with a moving phase boundary
and heat flow added from below (Oldenburg, 1975). This same
model can be used to explain the rapid uplift of the seafloor
topography at the southeast end of the Hawaiian chain and also
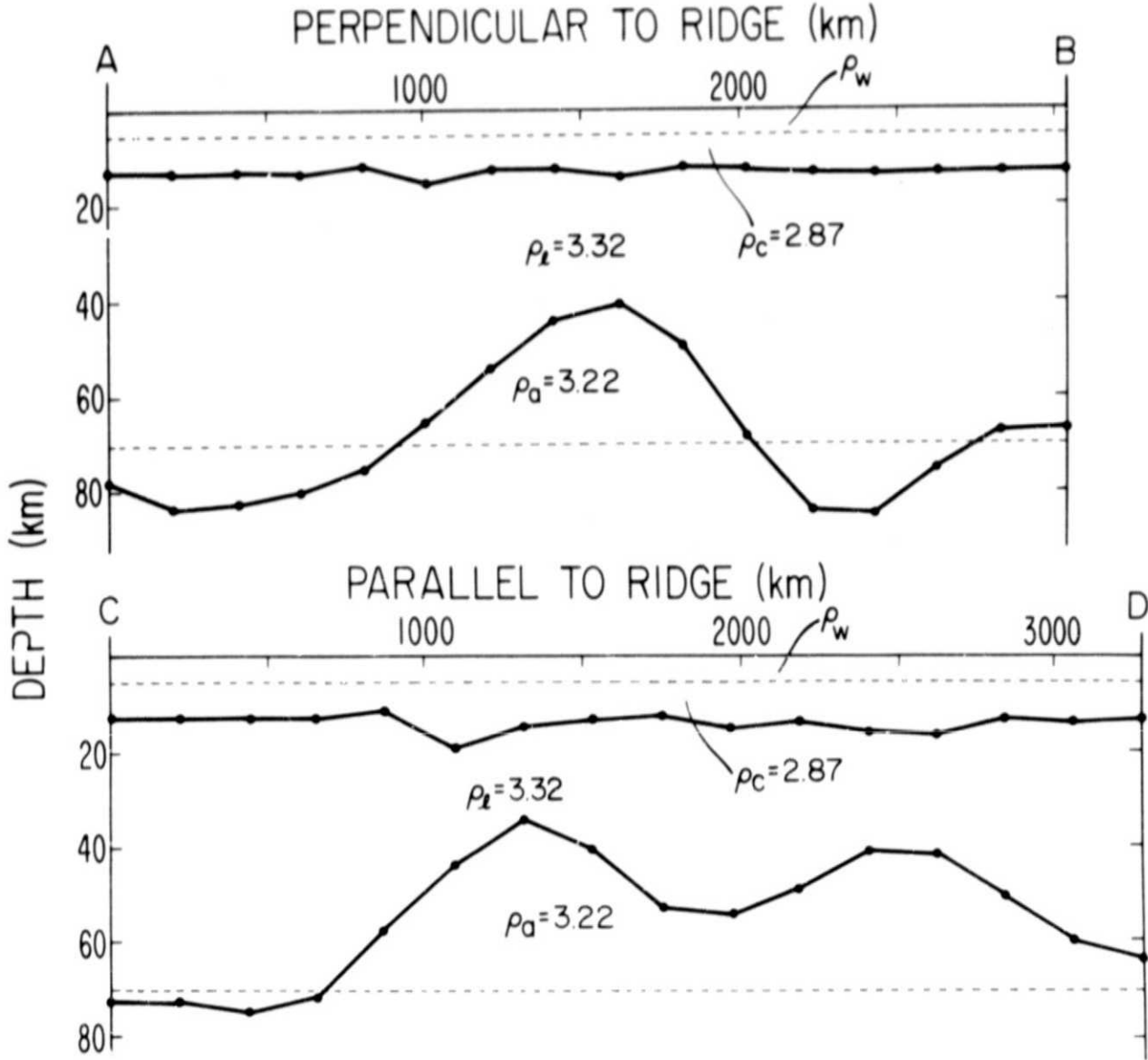the gradual subsidence of the older islands.

Figure 12. Cross sections of the Hawaiian chain assuming Airy compensation (Fig. 8). Tracks A-B and C-D are shown on Fig. 6. In each cros. section, the top dotted line is the mean ocean depth, the top solid line is the crust/lithosphere interface, and the bottom solid line is the lithosphere/asthenosphere interface.

Within the solid lithosphere the temperature is governed by the usual heat conduction equation

$$\frac{\partial T}{\partial t} = K \frac{\partial^2 T}{\partial z^2} \tag{3.3}$$

with an upper boundary condition of $T(0,t) = 0$ and $T(Z(t),t) = T_a$ at the lower boundary. The bottom boundary location is defined by the continuity relation

$$k \frac{\partial T}{\partial z}\Big|_{Z(t)} + \rho f L \frac{\partial Z(t)}{\partial t} = H_b(t) \tag{3.4}$$

where K is the thermal diffusivity, k the thermal conductivity, ρ the density of the solid, L the latent heat of fusion, f the fraction of material melted, T_a the solidus temperature, and $H_b(t)$ the heat flow into the base of the lithosphere (a function of time). Since we are not interested in the temperature solution for very young ages, horizontal heat flow has been ignored.

A solution to this set of equations was obtained by a finite difference method utilizing Lagrangian interpolation formulae similar to those described by Crank (1956). The bottom heat flow (H_b) largely determines the rate and direction of phase boundary movements. Taking $H_b = 0$, we could check our results with an analytic solution (Carslaw and Jaeger, 1959). Depth intervals of 1 km and time intervals of 2500 years were found to be adequate to reproduce the analytic result. For $H_b > 0$ and constant in time all solutions were found to asymptotically approach a constant surface heat flow given by $q_s(t=\infty) = kT_a/Z(\infty) = H_b$.

To simulate the heat advected to the base of the lithosphere by a plume we assumed a Gaussian shaped heat anomaly with a center at time t_p and a half width of 2.34σ where t_p is the time when the heat anomaly is a maximum, and σ is a variable parameter that determines the width of the anomaly. The position of the phase boundary and the surface heat flow were calculated for a number of bottom heat functions. The first bottom heat function used was $H_b(t) = H_o$. By changing the heat function to $H_b(t) = H_o + H_p \exp(-.5(\frac{t-t_p}{\sigma})^2)$, we found that the phase boundary would rapidly thin to a maximum thinning at a time less than 5 my after the heat flow maximum and then gradually thicken at later times. Figure 13 shows the position of the phase boundary and the surface heat flow as a function of time for the two different bottom heating functions. Values used in these models were $H_o = 0.65$ HFU, $H_p = 3.2$ HFU, $t_p = 90$ my and $\sigma = 3$ my. This thinning mechanism produces only a slight perturbation to the normal surface heat flow with a maximum deviation in surface heat flow occurring about 25 my after the plume is introduced.

The thinning data on Figure 12 can be approximated by this model if several assumptions are made. First, we have assumed that the thermal signature of the heat sources is Gaussian. Other functions can be assumed. Secondly, since the anomalous heating parameters necessary to account for the thinning depend upon the "normal" thermal structure of the lithosphere, some thermal model for the oceanic lithosphere must be assumed. The model assumed is that in Figure 13 with $H_b(t) = H_o = 0.65$ HFU and 5% partial melting. The model is somewhat arbitrary, but it does match the empirical surface heat flow and topography versus age relations (Parsons and Sclater, 1977). The actual lithosphere would be difficult to model in this area because the gradient of lithospheric age is almost perpendicular to the present direction of plate motion.

Figure 14 compares the model results with the thinning of Figure 12. The rapid thinning is easily accounted for by
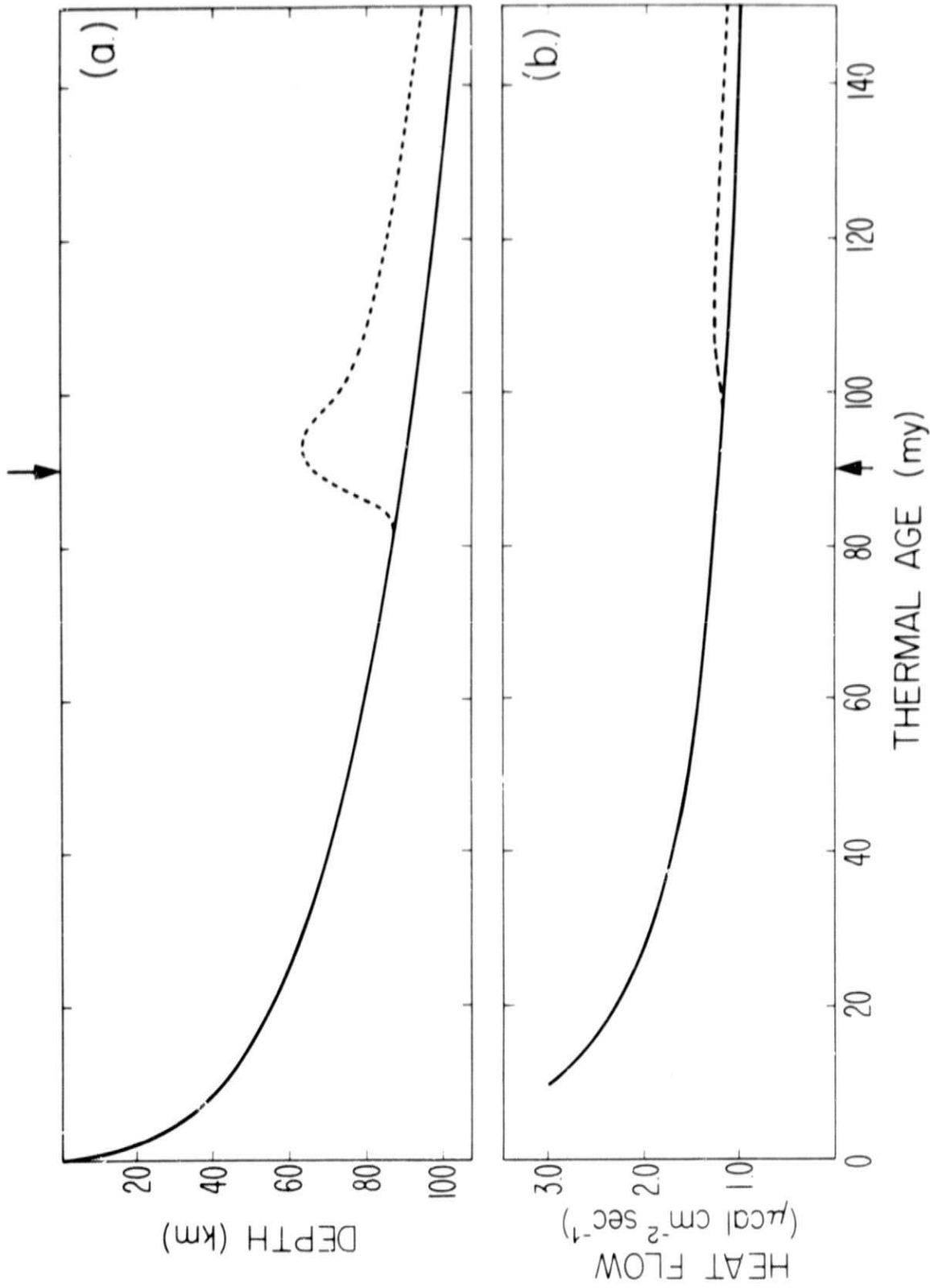
Figure 12. a) Phase boundary (solid line) as a function of time, using $K = .008 cm^2 sec^{-1}$, $k = .007 cal cm^{-1} sec^{-1} {}_oC^{-1}$, $\rho = 3.3 gm/cm^3$, $H_b = .65$ HFU, $f = .05$, $L = 100 cal gm^{-1}$. The dashed line is the phase boundary with a plume at $t_p = 90$ my. b) Surface heat flow as a function of time for the two $H_b(t)$.
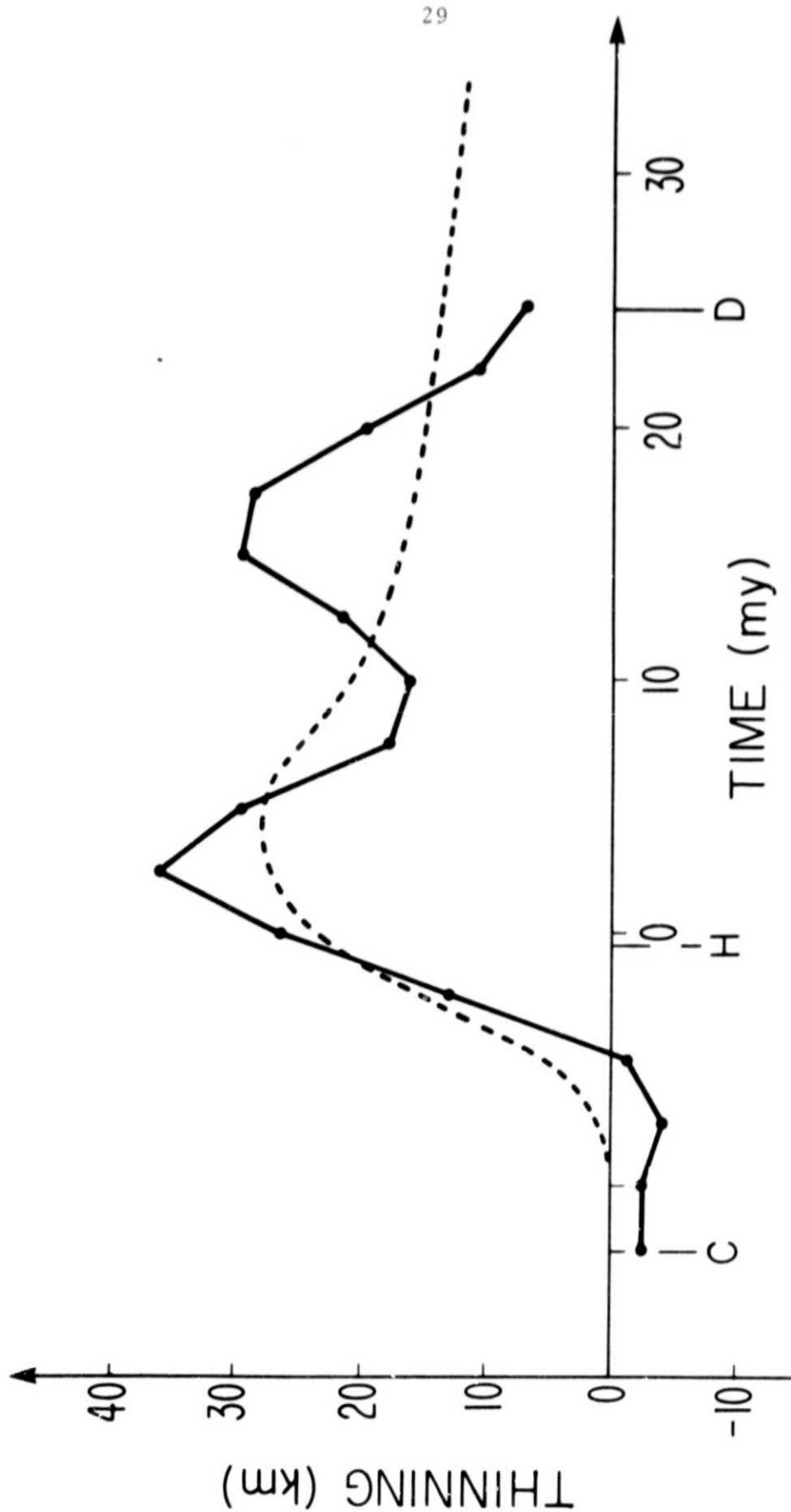
Figure 14. Solid line is the position of the lithosphere/asthenosphere boundary with respect to the mean position for the total area. Dotted line is the thinning caused by introduction of a heat anomaly at time = 0. Thinning is the same as Fig. 10. Profile C-D was converted from distance to time by using a plate velocity of 8.9 cm/yr. H marks the position of Hawaii.

the model as well as the later thickening. Ages are calculated
from Hawaii assuming a plate velocity of 8.9 cm/yr (Minster
et al., 1974). An interesting but maybe coincidental feature
of the model is that a good fit is obtained by moving the heat
flow maximum directly beneath Hawaii. Notice also that the
maximum thinning occurs about 5 my after the heat flow maximum.
It is also evident that the simple shape assumed for the heat
anomaly does not completely reproduce the details of the thinning.

3.4 Concluding Remarks

We have shown that the portion of the geoid that is co-
herent and in phase with the topography can be accounted for
by an Airy isostatic model with a compensation depth of 50-90
km. The lithospheric thinning predicted by the Airy model is
consistent with the observed subsidence of the island chain.
The rapid thinning of the lithosphere under Hawaii predicted by
the topography is easily accommodated by an increased heat flow
from the mantle. A thermal model has been developed which
predicts the movement of a phase boundary due to advected heat.

Lithospheric thinning and anomalous mantle heat flow may
account for other areas of anomalous depth than Hawaii. Others
(Menard, 1973) have proposed that the dynamic forces are res-
ponsible for some depth anomalies. Local differences in mantle
heat flow can also explain the same depth anomalies. Haigh
(1973) suggested that variations in upper mantle temperatures
might account for depth anomalies in the North Atlantic; this
is just a slightly different approach to our heating anomalies.
If lithospheric thinning is called upon to explain regions of
anomalous depth in the oceans, mantle flow patterns need not
supply large supporting forces. There is currently no evidence
to suggest that heat flow from the mantle is locally or even
regionally uniform.

4. OCEANIC LITHOSPHERIC AND ASTHENOSPHERIC MODELLING

4.1 Analysis

In recent years, thermomechanical models have been developed
at UCLA which prescribe the velocity of a rigid lithosphere, and
analyze the resulting flow and temperature patterns in the
asthenosphere under different rheological, thermal, and mechanical
conditions: dependences of viscosity on temperature and stress,
distribution of heat sources, depth of return flow, etc.
(Schubert et al., 1976; Froidevaux et al., 1977; Schubert et al.,
1978). The principal observables predicted by these models
are the topography and the heat flow. In addition, the tempera-
ture distributions in the upper mantle should be reasonably
consistent with those inferred from seismic Q and V_s, and the
stresses should be reasonably compatible with rock strengths
measured in the laboratory.

In these models, the gravity anomaly Δg is not explicitly calculated since for computational convenience the upper boundary is taken as rigid. However, the topography is estimated from the pressure p' generated by the flow. The pressure p' in turn depends on the excess temperature at depth, $T-T_{ref}$. For the depth D of the ocean floor, with respect to a reference level D_{ref} (Schubert et al., 1976, eq. 4; Schubert et al., 1978, eqs. 27-29):

$$D-D_{ref} = \frac{-(p'-p'_{ref})}{g(\rho-\rho_{SW})}$$

$$= -\frac{\rho\alpha}{(\rho-\rho_{SW})}\int_{-\infty}^{0}(T-T_{ref})dy, \tag{4.1}$$

where α is the coefficient of thermal expansion. The gravity anomaly in turn will result from a combination of the mass excess $D-D_{ref}$ constituted by the topography plus the mass deficiency constituted by the density of thermal expansion $-\rho\alpha(T-T_{ref})$ at depth. For a wave number k (e.g., Garland, 1971, p. 173):

$$\Delta g_k = 2\Pi G[-\int_{D_{max}}^{0} e^{-ky}\delta\rho_k(y)dy$$

$$+\int_{-\infty}^{0} e^{-ky}\alpha\rho\,\delta T_k(y)dy] \tag{4.2}$$

where $\delta\rho_k$ and δT_k are the Fourier transforms with respect to x (the horizontal direction) of $\rho(y)-\rho_{SW}$ and $T-T_{ref}$ respectively. The wave number k corresponds to a spherical harmonic degree ℓ of ak, where a is the earth's radius. Hence to obtain the disturbing potential δV_k and geoid height N_k:

$$\Delta g_k = (ak-1)\delta V_k/a \tag{4.3}$$

and

$$N_k = a\Delta g_k/g(ak-1) \approx \Delta g_k/kg \tag{4.4}$$

To integrate eq. 4.2 for a specific flow model requires specification of its wave number spectrum k and for each wave number the corresponding contribution δT_k to the anomalous temperature $T-T_{ref}$, as a function of depth y. The models in Schubert et al. (1976, Fig. 7) for 10cm/yr spreading velocity suggest a form for $T-T_{ref}$ of:

$$\delta T = 200\sin\frac{y}{120\Pi}e^{-t/50}, \tag{4.5}$$

for t in My and y in km, y<120 km. The wave length λ is about 10^4 km, and hence the wave number $k = 2\Pi/\lambda$ is about 6×10^{-4} km^{-1}. The resulting gravity anomaly from eq. 4.2 is thus about +13 mgals, and the corresponding geoid height about 22 meters.

A more accurate result would be obtained by numerically integrating eq. 4.2, of course. Furthermore, the full solution of the problem requires consideration of the effective lower boundary, as emphasized by McKenzie (1977). It is planned to explore further the implications of different spreading rates, heat source distributions, and rheologies for the gravity field.

4.2 Average Oceanic Lithosphere

Preliminary results have been obtained for lithospheric admittances by integrating the thermal structure of the simplest $t^{1/2}$ lithospheric model (Oldenburg, 1975). The method, however, was found to have several shortcomings: 1) Extreme sensitivity to the seafloor topography requires that the crustal thermal structure be specified at close (50 m) vertical intervals. 2) Admittances for wavelengths shorter than 500 km are dependent upon the details of the ridge crest model. 3) Stability of the admittances is, of course, best for smaller horizontal grid spacings. Numerical results for thermal models are commonly only calculated at large horizontal spacings to save money; the models must then be interpolated, thus introducing in-accuracies.

Since both gravity and bathymetry vary as $t^{1/2}$ except at the ridge crest and very far from the ridge crest, it is expected that the admittance will be nearly constant with wavelength. The slight deviations from $t^{1/2}$ at old ages will affect the largest wavelengths. The extent to which the long wavelengths differ from a constant will depend upon the length of the pro-file; longer wavelengths should have smaller admittances as gravity appears to flatten out more than bathymetry after 80 my. If admittances are calculated using the empirical free-air gravity and bathymetry vs. age relations of Cochran and Talwani (1977) the smaller admittances at longer wavelengths cannot be discriminated. The slopes of the $t^{1/2}$ lines for gravity and bathymetry indicated admittances of about 0.01 mgal/m, however, Fourier analysis reveals admittances closer to 0.008 mgals/m with a few larger than 0.01 mgal/m. The discrepancy can result either from the instability of the Fourier transform or from the gross averaging of the data, the former being the more likely. In either case, the value of 0.007-0.01 mgal/m is quite comparable to that obtained from a typical lithosphere model (Oldenburg, 1975); however, no wavelength variation can be reliably discerned.

The application of admittances to the thermal evolution of the lithosphere will prove to be beneficial only if reliable data can be obtained for comparison. Few places exist in the oceans where continuous profiles can be obtained from a ridge crest to very old lithosphere and it is this very old lithosphere that contains the information regarding deviations from the $t^{1/2}$ variations. If a profile is to be pieced together, care must be taken to assure that no absolute changes in gravity or bathymetry are incorporated into the profile.

REFERENCES

Balmino, G., K. Lambeck, & W.M. Kaula (1973). A spherical harmonic analysis of the earth's topography. J. Geophys. Res. 78:478-481.

Burkhard, N.R. & D.D. Jackson (1977). The shape of the low velocity channel beneath the Pacific. J. Geophys. Res. submitted.

Carslaw, H.S. and J.C. Jaeger (1959). Conduction of Heat in Solids. Oxford Univ. Press.

Chase, T.E., H.W. Menard, & J. Mammerickx (1970). Bathymetry of the North Pacific. Institute of Marine Resources, La Jolla, California.

Cochran, J.R. and M. Talwani (1977). Free-air gravity anomalies in the world's oceans and their relationship to residual elevation. Geophys. J. Roy. Astr. Soc 50: 495.

Crank, J. (1957). Two methods for the numerical solution of moving-boundary problems in diffusion and heat flow. Quat. J. Mech. Appl. Math. 10:220-230.

Crough, S.T. and G.A. Thompson (1976). Numerical and approximate solutions for lithospheric thickening and thinning. Earth Planet. Sci. Lett. 31:397-402.

Detrick, R.S. and S.T. Crough (1978). Island subsidence, hot spots, and lithospheric thinning. J. Geophys. Res. 83: 1236-1244.

Ewing, J., M. Ewing, T. Aitken, and W.J. Ludwig (1968). North Pacific sediment layers measured by seismic profiling. In Geophys. Mono. 12. Amer. Geophys. Un.

Ewing, M., R. Houtz and J. Ewing (1969). South Pacific sediment distribution. J. Geophys. Res. 74:2477.

Froidevaux, C., G. Schubert, & D.A. Yuen (1977). Thermal and mechanical structure of the upper mantle: a comparison between continental and oceanic models. Tectonophysics 30:233.

Haigh, B.I.R. (1973). North Atlantic topography and lateral variations in the upper mantle. Geophys. J. R.A.S. 33:405-420.

Heron, E.M. (1972). Seafloor spreading and the Cenozoic history of the east central Pacific. Bull. Geol. Soc. Amer. 83:1671.

Hilde, T.W.C., N. Isezaki and J.M. Wageman (1976). Mesozoic seafloor spreading in the North Pacific. In Geophys. Mono. 19, Amer. Geophys. Un., pp. 205-226.

Hussong, D.M. (1972). Detailed structural interpretations of
    the Pacific oceanic crust using ASPER and ocean-bottom
    seismometer methods. Ph.D. dissertation, 165 pp., Univ.
    of Hawaii.

Kaula, W.M. (1977). Geophysical inferences from statistical
    analyses of the gravity field. Proc. Int. Symp. "The
    Changing World of Geodetic Science". Ohio State Univ.,
    Dept. Geod. Sci. Rep. 250:119.

Kaula, W.M. (1978). Extensions of the theory of statistical
    analyses on a sphere. Bull. Geod. Sci. Aff. 37:521-531.

Larson, R. and C. Chase (1972). Late Mesozoic evolution of
    the Western Pacific Ocean. Bull. Geol. Soc. Amer.
    83:3627.

Larson, R. and T. Hilde (1975). A revised time scale of magnetic
    reversals for the early Cretaceous and late Jurrassic.
    J. Geophys. Res. 80:2586.

Mammerickx, J., S. Smith, I. Taylor, and T. Chase (1975).
    Bathymetry of the South Pacific. Institute of Marine
    Resources, La Jolla, California.

Matthews, D.J. (1939). Tables of the velocity of sound in
    pure water and seawater for use in echo-sounding and
    sound-ranging. H.D. 282, 52 pp., Hydrogr. Dep., Admiralty,
    London.

McKenzie, D.P. (1967). Some remarks on heat flow and gravity
    anomalies. J. Geophys. Res. 72:6261.

McKenzie, D.P. (1977). Surface deformation, gravity anomalies
    and convection. Geophys. J. Roy. Astr. Soc. 48:211.

McKenzie, D.P. and C. Bowin (1976). The relationship between
    bathymetry and gravity in the Atlantic Ocean. J. Geophys.
    Res. 81:1903.

McKenzie, D.P., J.M. Roberts and N.O. Weiss (1974). Convection
    in the earth's mantle: towards a numerical simulation.
    J. Fl. Mech. 62:465.

Menard, H.W. (1973). Depth anomalies and the bobbing motion
    of drifting islands. J. Geophys. Res. 78:5128-5138.

Minster, J.B., T.H. Jordan, P. Molnar, and E. Haines (1974).
    Numerical modelling of instantaneous plate tectonics.
    Geophys. J. R.A.S. 36:541-576.

Oldenburg, D.W. (1975). A physical model for the creation of the
    lithosphere. Geophys. J. R.A.S. 43:425-451.

Parsons, B. and J.G. Sclater (1977). An analysis of the variation of ocean floor heat flow and bathymetry with age. J. Geophys. Res. 82:803.

Schubert, G., C. Froidevaux, & D.A. Yuen (1976). Oceanic lithosphere and asthenosphere: thermal and mechanical structure. J. Geophys. Res. 81:3525.

Schubert, G., D.A. Yuen, C. Froidevaux, L. Fleitout, & M. Souriau (1978). Mantle circulation with partial return flow: effects on stresses in oceanic plates and topography of the seafloor. J. Geophys. Res. 83:745-758.

Sclater, J.G., L.A. Lawver, and B. Parsons (1975). Comparison of long-wavelength residual elevation and free-air gravity anomalies in the North Atlantic and possible implications for the thickness of the lithospheric plate. J. Geophys. Res. 80:1031.

Smith, D.E., F.J. Lerch, J.G. Marsh, C.A. Wagner, R. Kolenkiewicz, and M.A. Khan (1976). Contributions to the National Center. J. Geophys. Res. 81:1006-1026.

Walcott, R.I. (1970). Flexure of the lithosphere at Hawaii. Tectonophysics 9:435-446.

Watts, A.B. (1976). Gravity and bathymetry in the central Pacific Ocean. J. Geophys. Res. 81:1533.

1. Report No. NASA CR-156854	2. Government Accession No.	3. Recipient's Catalog No.
4. Title and Subtitle Studies of Oceanic Tectonics Based on GEOS-3 Satellite Altimetry		5. Report Date November 1978
		6. Performing Organization Code
7. Author(s) K. A. Poehls, W. M. Kaula, G. Schubert, D. Sandwell		8. Performing Organization Report No.
		10. Work Unit No.
9. Performing Organization Name and Address Department of Earth and Space Sciences University of California Los Angeles, California 90024		11. Contract or Grant No. NAS6-2463
		13. Type of Report and Period Covered Final Report
12. Sponsoring Agency Name and Address National Aeronautics and Space Administration Wallops Flight Center Wallops Island, Virginia 23337		14. Sponsoring Agency Code

15. Supplementary Notes

16. Abstract

The interpretation of the ocean geoid has been pursued by statistical analyses of altimetry and topography; the application of inverse theory to the geoid in combination with topographic and seismic data; and the development of mantle flow models.

In the statistical analyses, we have compared the geoidal admittance (relationship between the ocean geoid and seafloor topography) obtained from GEOS-3 altimetry to various model admittances. Analysis of several altimetry tracks in the Pacific Ocean demonstrates a rather low coherence between altimetry and seafloor topography except where the track crosses active or recent tectonic features. The general lack of coherence between geoid and topography suggests a partial or complete decoupling between the sources of the geoid anomalies and the lithospheric plate, possibly in the form of a low viscosity zone. Global statistical studies using the much larger data base of all available gravimetry do show a positive correlation of oceanic gravity with topography, predominantly in spherical harmonic degrees 3 through 6, but with an overall correlation coefficient of only 0.11. This result reflects the dominance of seafloor spreading.

The application of inverse theory has, up till now, been limited to feasibility studies. Burkhard and Jackson (1977) have modelled the oceanic lithosphere by simultaneously inverting surface wave dispersion, topography, and gravity data. They find both a lid and subchannel that vary in thickness with age. Efforts to incorporate geoid data into the inversion have shown that the base of the subchannel can be better resolved with geoid rather than gravity data. The use of geoid data is more difficult than gravity because geological features at much greater lateral distances are accounted for.

Thermomechanical models of seafloor spreading taking into account differing plate velocities, heat source distributions, and rock rheologies have been developed at UCLA in recent years. These models predict topography, heat flow, and temperature and stress variation with depth. Geoidal heights obtained by integrating over the temperature distribution and topography are on the order of 20 meters.

17. Key Words (Suggested by Author(s)) GEOS-3 geoid tectonics lithosphere	18. Distribution Statement Unclassified - unlimited STAR Category - 42,46,48		
19. Security Classif. (of this report) Unclassified	20. Security Classif. (of this page) Unclassified	21. No. of Pages 36	22. Price*